The Astrophysical Journal
Preprint typeset using LaTeX style emulateapj v. 12/16/11

HIGH CADENCE, HIGH RESOLUTION SPECTROSCOPIC OBSERVATIONS OF HERBIG STARS HD 98922 AND V1295 AQUILA

Alicia N. Aarnio[1*], John D. Monnier[1], Tim J. Harries[2], Stefan Kraus[2], Nuria Calvet[1], David Acreman[2] & Xiao Che[1]

(Accepted 20 August 2017)

ABSTRACT

Recent observational work has indicated mechanisms for accretion and outflow in Herbig Ae/Be star-disk systems may differ from magnetospheric accretion as it is thought to occur in T Tauri star-disk systems. In this work, we assess the temporal evolution of spectral lines probing accretion and mass loss in Herbig Ae/Be systems and test for consistency with the magnetospheric accretion paradigm. For two Herbig Ae/Be stars, HD 98922 (B9e) and V1295 Aql (A2e), we have gathered multi-epoch (∼years) and high cadence (∼minutes) high resolution optical spectra to probe a wide range of kinematic processes. Employing a line equivalent width evolution correlation metric introduced here, we identify species co-evolving (indicative of common line origin) via novel visualization. We interferometrically constrain often problematically degenerate parameters, inclination and inner disk radius, allowing us to focus on the structure of the wind, magnetosphere, and inner gaseous disk in radiative transfer models. Over all timescales sampled, the strongest variability occurs within the blueshifted absorption components of the Balmer series lines; the strength of variability increases with the cadence of the observations. Finally, high resolution spectra allow us to probe substructure within the Balmer series' blueshifted absorption components: we observe static, low-velocity features and time-evolving features at higher velocities. Overall we find the observed line morphologies and variability are inconsistent with a scaled-up T Tauri magnetospheric accretion scenario. We suggest that as magnetic field structure and strength change dramatically with increasing stellar mass from T Tauri to Herbig Ae/Be stars, so too may accretion and outflow processes.

1. INTRODUCTION

Herbig Ae/Be (HAeBe) stars are the high mass (∼2-10 $M_\odot$) pre-main sequence counterparts of T Tauri stars (TTS). Classically defined, they are spectral type A or earlier, show emission lines in their spectra, lie in obscured regions, and illuminate surrounding nebulosity (Herbig 1960). Being similar in evolutionary state and observed phenomena, these systems have often been treated as scaled-up TTS, magnetospherically accreting via strong, extended dipolar magnetic field components. Indeed, in some cases, magnetospheric accretion (MA) has been able to successfully reproduce observed spectral line profiles (Muzerolle et al. 2004). Recent spectropolarimetric surveys, however, have found a very low (∼10%) detection rate for magnetic fields on Herbig Ae/Be stars (Wade et al. 2007; Alecian et al. 2013c), and those detected have weaker dipole components than observed in TTS (∼100 G in HAeBe, as opposed to ∼1 kG for TTS). Indeed, moving to higher mass in the Hertzsprung-Russell diagram, the dipole moment is seen to weaken, and higher order moments dominate the overall field structure (Gregory et al. 2012); this effectively truncates the "reach" of the stellar magnetosphere in star-disk interaction and distributes the accretion footpoints about the stellar surface in a less-ordered manner.

At the same time, it has been shown that the few HAeBe stars with magnetic field detections are slower rotators than their non-magnetic counterparts, indicating effective braking has taken place somehow (Alecian et al. 2013b). In higher mass HAeBe systems (>5 $M_\odot$), Alecian et al. (2013b) showed substantial angular momentum loss occurs as they contract to the main sequence; the authors suggest increased wind mass loss as the driver of this. Mendigutía et al. (2011b) showed a clear break in the dependence of accretion indicators (Balmer excess, Hα line width) as a function of stellar mass, with Ae stars resembling TTS and Be stars not. Spectrointerferometric results have indicated that for late-type HAeBe systems, Brγ line emission is originating from within a few stellar radii of the star, consistent with a magnetospheric accretion paradigm (Kraus et al. 2008a,b; Ellerbroek et al. 2015). For earlier-type Herbigs, however, the origin of line emission is ∼1-6 au, consistent with a disk or X-wind (e.g., Weigelt et al. 2011; Kurosawa et al. 2016). Unfortunately, only a few systems have been observed via this technique.

While this is suggestive that later-type Herbigs accrete magnetospherically while earlier types accrete via different mechanisms (supported by spectropolarimetric observations of Vink et al. 2002), ambiguity remains: Kraus et al. (2008b) observe Brγ emission from within the dust sublimation radius in all of their targets regardless of spectral type, and these radii could be consistent with magnetospheric accretion, a stellar wind, or an X-wind. In only one case do Kraus et al. (2008b) suggest the compact Brγ emission line region, in concert with accretion indicators, to be likely indicating magnetospheric accretion: HD 98922. The modeling work of Caratti o Garatti

[1] Department of Astronomy, University of Michigan, 311 West Hall, 1085 S. University Ave., Ann Arbor, MI 48109
[2] Department of Physics and Astronomy, University of Exeter, Stocker Road, Exeter EX4 4QL, UK
[*] Now a Hale Fellow at the University of Colorado Boulder, 8665 Discovery Drive, Boulder, CO 80303

et al. (2015) is able to successfully reproduce the Brγ emission as originating from a disk wind launched over $\sim$0.1-1 au and a mass loss rate of $2\text{x}10^{-7}M_\odot$ yr^{-1}.

These observations counter the scaled up T Tauri magnetospheric accretion paradigm of a strong, extended dipole interacting with circumstellar material, and in concert with a lack of magnetic field detections in these objects, indicate a need to expand upon our picture of star-disk interaction in HAeBe systems.

Observations done in the time domain, sampling a range of dynamical timescales across the system, are critical for disentangling episodic, periodic (linked to rotation), and large-scale (disk-driven) processes' effect on observables, especially given the degeneracy in line formation mechanisms. Using high resolution, high signal-to-noise optical spectra, we compare the mass flux within two star-disk systems on both short and long timescales with the goal of determining whether relationships exist between accretion and outflow processes, on what timescales these happen, and whether the observations are consistent with the magnetospheric accretion paradigm as envisaged for lower mass pre-main sequence stars.

In Section 2 we describe our target selection and observations, and in Section 3 we describe our analysis of the data. Sections 4 and 5 share results and conclusions, and in Appendices A, B, and C, we present an atlas of our spectra, radiative transfer models, and further details of our correlation analysis methods.

2. TARGET SELECTION AND OBSERVATIONS

From 2006 to 2013, we conducted an optical spectroscopic observational campaign of a sample of $\sim$60 HAeBe stars. Our target sample consists of stars for which we either already have interferometric data or targets that would be suitable for interferometric observation (i.e., bright; $\sim V < 14$, $H < 8$). These targets are ideal for modeling as the interferometric data break degeneracies that create ambiguity in interpretation (e.g., inclination and inner disk radius). Over the course of gathering data, we observed 13 objects at multiple epochs; two of these, V1295 Aql and HD 98922, were followed up on in 2013 with high cadence time series observations. V1295 Aql and HD 98922 were chosen for follow up observation because they occupy and extend into the range of stellar masses (2.9 and 5.0$M_\odot$, respectively) in which trends in mass accretion rate and line luminosity break from those observed in TTS (Mendigutía et al. 2011b). Also of particular interest, these stars represent magnetic V1295 Aql and non-magnetic HD 98922 examples to compare and contrast.

Our optical spectra were taken with MIKE (Bernstein et al. 2003), the Magellan Inamori Kyocera Echelle, a cross-dispersed double échelle spectrograph. The blue side of MIKE covers a $\sim$3200$-$5000Å range, and the red chip spans $\sim$4900$-$10000Å; using the narrowest slit, 0."35, the resolving powers of the blue and red sides are R$\sim$80,000 and R$\sim$65,000, respectively. Within this wavelength range, we simultaneously capture many well-studied MA and outflow tracing lines, including the Balmer discontinuity, Hydrogen Balmer series lines, Na D doublet, He I 5876Å line, Ca II infrared triplet, and [O I] 6300Å line.

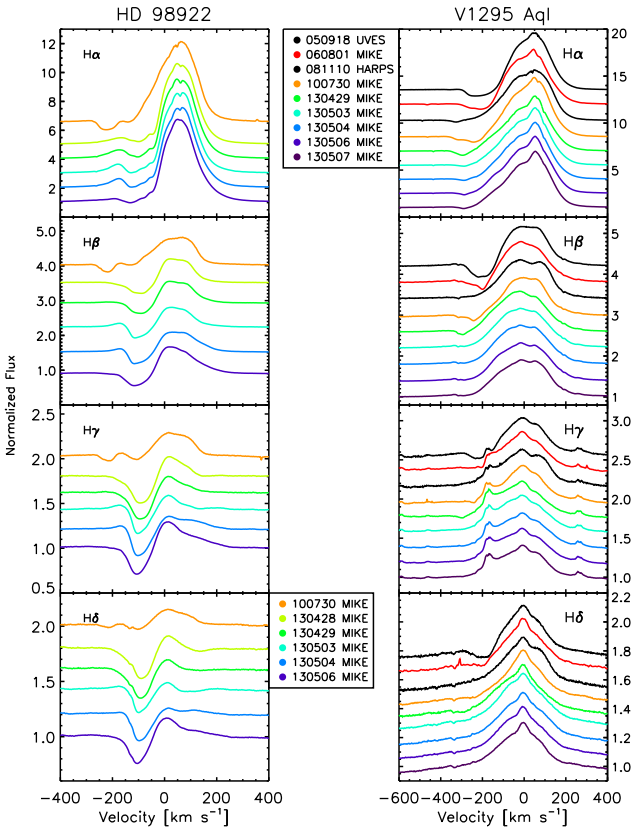

FIG. 1.— Continuum-normalized spectra for HD 98922 and V1295 Aql: evolution of the Balmer series lines. Stellar photospheric absorption has been removed from the spectra. Mean spectra are shown in progressing date order from top to bottom; all available epochs from both our MIKE data (color-coded by date) and the literature (black) plotted here with arbitrary offsets for display purposes. UT dates in the legends are in YYMMDD format. V1295 Aquila's Hγ line shows contamination from four strong Fe I lines at -157, 1.2, 90, and 277 km s^{-1}.

For six nights in a ten-day period, we observed the targets in $\sim$1 hour long visits, taking spectra at as high temporal resolution as possible while obtaining adequate signal. Our final data set is comprised of 111 blue and 132 red spectra for HD 98922, and 75 blue and 95 red spectra for V1295 Aql. The cadence of these observations is $\sim$3 minutes for HD 98922 (read-out limited), and $\sim$4.5 minutes for V1295 Aql. The log of our observations is reported in Table 1. We show the mean profiles for each night, plus earlier epochs of observation with MIKE, in Figure 1.

3. ANALYSIS

For the basic spectral reduction process, flat fielding, trimming and bias subtraction, background removal, and boxcar extraction, we employed the MIKE IDL pipeline (Bernstein et al. 2015). Post-pipeline tools written by us further removed the blaze and continuum, and merged the échelle orders. Our blaze/continuum removal procedure fit a weighted surface to the extracted échelle orders to preserve broad line wings.

To obtain radial velocities, we cross-correlated mean spectra from each night with synthetic templates from Munari et al. (2005). We used Fe II, Ti II, Cr II, and Mg II lines as described in Mora et al. (2001) to deter-

TABLE 1
Time series observing log

Object ID	UT Start [hh:mm:ss]	Blue/Red Side	Integration Time [s]	Airmass
2005 September 18, UVES archival spectra				
V1295 Aql	01:25:49.04	6650−10250Å	200	···
V1295 Aql	01:25:53.13	3044−3916Å	360	···
V1295 Aql	01:25:53.13	3732−4999Å	175	···
V1295 Aql	01:34:59.91	4726−6835Å	160	···
2006 August 01, 1" slit, 1x3 binning, slow readout				
V1295 Aql	07:53:32	B	50	2.325
V1295 Aql	07:57:19	B	25	2.392
V1295 Aql	07:58:38	B	25	2.416
V1295 Aql	07:53:33	R	50	2.325
V1295 Aql	07:57:19	R	25	2.392
V1295 Aql	07:58:45	R	25	2.418
V1295 Aql	08:03:22	R	50	2.509
2008 November 10, HARPS archival spectra				
V1295 Aql	23:48:09	3781−6912Å	600	1.527
V1295 Aql	23:58:42	3781−6912Å	600	1.586
2008 November 11, HARPS archival spectra				
V1295 Aql	00:09:15	3781−6912Å	600	1.653
V1295 Aql	00:19:47	3781−6912Å	600	1.730
V1295 Aql	00:30:19	3781−6912Å	600	1.819
V1295 Aql	00:40:52	3781−6912Å	600	1.922
V1295 Aql	00:51:25	3781−6912Å	600	2.042
V1295 Aql	01:01:58	3781−6912Å	600	2.185
2010 July 30, 1x1 binning, fast readout				
HD 98922	23:40:52	B	15	1.564
HD 98922	23:45:49	B	80	1.588
HD 98922	23:48:49	B	80	1.604
HD 98922	23:51:56	B	80	1.621
HD 98922	23:54:53	B	80	1.637
HD 98922	23:40:54	R	15	1.564
HD 98922	23:45:50	R	40	1.588
HD 98922	23:47:52	R	40	1.599
HD 98922	23:50:12	R	40	1.611
HD 98922	23:53:19	R	40	1.628
HD 98922	23:56:20	R	40	1.645
··· Table can be viewed in full in online data ···				

Note. — Multi-epoch and time-series observations of HD 98922 and V1295 Aquila. All data are MIKE spectra, unless otherwise indicated. Time-series spectra were generally taken in sets of four integrations, with ThAr lamps taken between sets.

mine the $v\sin i$ for each star. Finally, we removed stellar photospheric absorption by subtracting a continuum-normalized, high-resolution synthetic spectrum (Munari et al. 2005).

To quantitatively assess line variability, we calculated normalized variance profiles (Johns & Basri 1995), which measure the variance in a given line's velocity bins across all spectra observed. In Figure 2 we show the variance of HD 98922 and V1295 Aql's Hα lines with respect to the mean line profile over all epochs of available data (spanning years) as well as with respect to the mean line profile across the entire week of observation in 2013. In both cases, the variance is greater over the longer time baselines sampled. V1295 Aql is more strongly variable than HD 98922 over both short and long-term observing windows; we note in Section 4 physical changes observed in V1295 Aql over this timescale that could be responsible.

To assess contributions of distinct components, we employed PAN, Peak ANalysis[4], to fit our line profiles with a series of Gaussian functions. In principle, a model with arbitrarily many components could fit the data well; to guard against overfitting the line profiles, we calculated

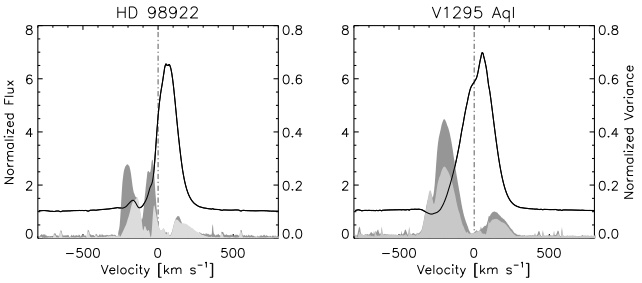

Fig. 2.— Hα variability: mean profiles (solid lines) and normalized variance profiles (filled) for HD 98922 (left) and V1295 Aql (right). Dark shaded regions are the variance profiles over all epochs of observation, while the lighter filled areas represent the variance profiles over our five nights of observation in 2013. The left axis of ordinates denotes the normalized flux of the mean Hα profiles (solid, black lines), while the right axis of ordinates marks the variance profiles' (filled, solid) value.

[4] PAN was written by Rob Dimeo at the NIST Center for Neutron research and based upon activities supported by the National Science Foundation under Agreement No. DMR-0086210.

the F-statistic of each fit and did not add additional components if they did not statistically significantly improve the fit. In the case of Hα, the line complexity and strength made fits with relatively few components indistinguishable from one another; in these cases, we proceeded with as few components as possible to obtain a qualitatively good fit. As an arbitrarily large number of Gaussian components could certainly reduce the χ^2 value of the fit, we rely on the F-statistic to ensure we are not overfitting and only refer to the emission and absorption components in general terms. Within the PAN gui, in order to avoid unrealistic and spuriously large (though statistically equivalent) component fits, we set limits on the Gaussian components' widths, areas, and central wavelengths; in cases where components weakened to non-detection, these components' areas are allowed to go to 0. If any parameter reached the imposed limit, we re-expanded the allowed range and re-fit. We present examples of fits to the Hα profiles of HD 98922 and V1295 Aql in Appendix C.

Having fit our spectral lines, we then measured the equivalent widths (EWs) of the emission and wind absorption components of 26 species and calculate the correlation of their variability relative to one another: should we see strongly correlated or anti-correlated behaviors, it could be indicative of a common timescale for evolution of the line feature and thus potentially a common origin. The correlation coefficient we employ here is Spearman's ρ (Press et al. 1992); we note that this statistic gauges linear relationships between monotonically increasing quantities; this is not always the case with our data. When the data are significantly non-monotonic, however, the coefficient approaches zero and the two-sided significance is large (here, we use 10^{-3} as a cutoff), meaning it is probable that unrelated variables could produce this level of correlation and thus it is not statistically significant. These results are shown in Figures 3 and 4.

Finally, we have run preliminary fiducial radiative transfer models using the TORUS code (Transport Of Radiation Under Sobolev/Stokes; Harries 2000). We employ a simple dipolar field geometry, a split-monopole style disk wind (Knigge et al. 1995; Long & Knigge 2002), and calculate line transport in the Balmer series to compare to observations. We describe details of the parameter choices and model physics in Appendix B and discuss general findings in the following sections.

4. RESULTS

Over the broad wavelength range observed with MIKE, we have detected and measured the permitted transitions of Hα, Hβ, Hγ, Hδ, He I 5875Å, Na I 5889Å, Na I 5895Å, He I 6678Å, O I 8446Å, Ca II IR triplet (8498Å, 8542Å, 8662Å), O I 7772Å, Fe II (42) multiplet (4923Å, 5018Å, 5169Å), and Ca II H and K (3933Å, 3968Å). We have also detected and measured the forbidden transitions of [O I] 5577Å, [O I] 6300Å, [O I] 6363Å, [Ca II] 7323Å, [Fe II] 7155Å. At MIKE's high resolution, we note a wealth of substructure in the blueshifted line absorption wings observed, including three distinct velocity minima within the P Cygni profile in Hα for HD 98922 (we explore this substructure further in Section 4.2). Plots of these transitions can be found in Appendix A.

Assuming the observed Balmer jump excess and Brγ emission are produced via MA, accretion rates have been estimated for both V1295 Aql ($\sim10^{-5}$ $M_\odot$ yr^{-1}, Mendigutía et al. 2011b) and HD 98922 ($\sim10^{-6}M_\odot$ yr^{-1}, Garcia Lopez et al. 2006). In contrast to accreting TTS, we do not see any redshifted absorption; Hartmann et al. (1994) note that at the high velocities found in accretion flows Hα can thermalize, thereby filling in the telltale inverse P Cygni absorption. If present, however, we should observe redshifted absorption in the higher order Balmer lines as they do not thermalize; for neither object do we see redshifted absorption indicative of magnetospheric accretion-related infall in any transition we observed. Cauley & Johns-Krull (2014) observed the He 10830Å transition in V1295 Aql and also noted only blueshifted absorption. In our fiducial TORUS models for both stars, we are unable to produce any line profile invoking MA that does not have an inverse P Cygni profile in all of the Balmer lines (see Appendix B for further detail).

We do not observe a high velocity component of the [O I] 6300Å line frequently seen in TTS systems (e.g., Hartigan et al. 1995), and thus have not estimated wind mass loss rates. In HAeBe systems, this feature is rare: Acke et al. (2005) pointed out that in their sample of 49 HAeBe stars, only 3 showed any high velocity [O I] 6300Å feature.

Variability in spectral lines is related to the emitting or absorbing volume being probed by the line and its dynamical properties. At the shortest timescales, of order minutes to hours, we are probing regions close to the stellar surface: accretion flows, the launching region of a stellar wind, episodic mass loss and the rotational modulation of any of these events. Longer timescales, of order days to weeks, probe regions between the star and disk, from corotation to fractions of an au. In these regions, we may observe variability related to extended magnetospheric structure, hot gaseous inner disk components, and magnetospheric ejections (cf. Ferreira et al. 2006; Ferreira 2013). The longest timescales, of order months to years, probe inner disk Keplerian orbital times.

While we do note low, $\sim$5% level, variability over the course of our hour-long observations, the strongest variability we observe occurs on timescales of days or longer; years for V1295 Aql. In both objects, the most variability on any timescale occurs in the blueshifted absorption components. In contrast to TTS variability observations, we see little change in the overall emission level or the red wings of our lines; what variability we observe in the red line wings appears to be due to modest overall change in the width of the line (consistent with the results of Mendigutía et al. 2011a). The most dramatic spectrum-to-spectrum changes occur on the longest time baselines available to us, over years, and are dramatic shifts in the blueshifted absorption component velocity. Studies of line profile variability in TTS and IMTTS (e.g., Johns & Basri 1995; Costigan et al. 2014; Sousa et al. 2016) have found substantial amounts of variability across the line profile, including at redshifted velocities. Nguyen et al. (2009) and Costigan et al. (2014) find variability in TTS and Herbig Ae stars saturates at the rotation period.

Quantitatively assessing variability over the full set of observations, Figures 3 and 4 readily allow for compari-

son between V1295 Aql and HD 98922. Each square in the diagram represents how any given two line components evolve in time with respect to each other; for reference, we show specific examples in Appendix C. In both stars, singly ionized species show more variability, both anti- and correlated with other singly ionized species, than the neutrals during the ∼10 day long period sampled. This implies the singly ionized species originate in a compact region evolving on short timescales. We also see that in both stars species in the same multiplet, e.g., Fe II (42), have positively correlated time evolving behavior, as expected under an assumption of a common origin of these lines. Similarly, lines of the same multiplet share common time-series evolution when compared with other lines. Interestingly, in V1295 Aql, the emission and absorption components of lines with P-Cygni profiles show anticorrelated time evolution, whereas the components evolve together for HD 98922. Unlike what is seen in HD 98922, for V1295 Aql we note little correlation between forbidden line evolution and the neutral and singly-ionized species selected; we note that our method is insensitive to potential time delays, this method is biased toward short timescale co-evolution. In forthcoming work, we will use radiative transfer modeling to explore further the conditions that would cause anticorrelated versus correlated evolution of components in the same line.

4.1. *V1295 Aql*

In Table 2, we summarize stellar parameters for V1295 Aql. Its magnetic field, ∼100G, has been detected and confirmed by multiple authors over several years (Alecian et al. 2013c; Hubrig et al. 2006, 2009; Catala et al. 2007) and one non-detection was reported by Wade et al. (2007). As described in Section 3, from our MIKE spectra we measure v_r = -1.2±1.3 km s^{-1} and $v\sin i$ =3.19±2.45 km s^{-1}, consistent with Alecian et al. (2013c). With these parameters and assuming star and disk share an inclination of 34±2° (Lazareff et al. 2017), we derive a rotation period of ∼32d. As Alecian et al. (2013b) note, the handful of magnetic HAeBe stars observed are also slow rotators, consistent with V1295 Aql's apparently very slow rotation rate.

For the observations spanning multiple years, we see the P Cygni absorption is consistently growing weaker. In our first nights of data, in 2005 and 2006, blueshifted absorption is detectable in Hα, Hβ, Hγ and Hδ, but can only be seen in Hα and Hβ thereafter (Fig. 1); simultaneously, the emission component's EW is also growing weaker. The Ca II infrared triplet is also dramatically weakening, as are the Na I D lines. The Ca II H and K lines, notable for their complex structure (cf. Pogodin et al. 2005, and references therein), are not seen to vary much on night-to-night timescales, or within any given night (this is consistent with previous observations; in In Appendix A we show plots of all of these lines). Alecian et al. (2013a) note spectropolarimetric changes indicating V1295 Aql had a stable, aligned dipole over observations from 2004-2009, but in 2011-2012, variability was observed, indicating a change in the star's magnetic field structure. In 2005 and 2006 data, we see broad P-Cygni absorption, and in 2008 data, we only note a weak, higher velocity absorption feature. In 2010, a broad, multi-trough component appears, only to have disappeared again by our 2013 data taken for this work. The correlation between magnetic field structure and the Hα profiles is unclear, but we note in the epochs with weak absorption, the emission component's width has broadened, possibly filling in underlying absorption.

[O I] 6300Å in particular is of interest, as its driving mechanism remains unclear. Using multi-epoch data, Corcoran & Ray (1998) noted a relationship between the [O I] emission and presence of near-IR excess; they suggested the IR excess was indicative of accretion. Line component analysis of our time-series data finds the Hα wind absorption component is weakly anticorrelated with the [O I] emission: over the period of observation, the [O I] 6300Å emission line grew stronger as the wind absorption in Hα grew weaker. To quantitatively assess the line components' evolution, we calculated Spearman's correlation coefficient for time-series equivalent widths: comparing [O I] emission and blueshifted absorption in Hα, the test statistic ρ is -0.39 with a significance of 8x10^{-5}; this is to say the likelihood of a spurious correlation is very small, and this is a statistically significant result. In contrast, ρ for the emission component of Hα and the [O I] EW is -0.09 with a significance of 0.37, which does not fall below the adopted 10^{-3} threshold for significance.

The timescales on which the blueshifted absorption in Hα and Hβ varies, ∼1 day, are more consistent with regions close to the star; the velocity center of the absorption is consistent with the (de-projected) stellar escape velocity, ∼300 km s^{-1}. Indeed, earlier authors have suggested the narrow line widths and line symmetry suggest heating at the base of a stellar wind launching region as the origin of metallic line emission (Catala et al. 2007). Asymmetries in these metallic lines are attributed to obscuration of the emitting region by the wind (Pogodin et al. 2005). At the relatively low system inclination, a high degree of collimation/small opening angle would be necessary in order for material to be present along the line of sight; this is easier to accomplish with a stellar wind than a disk wind. Indeed, our initial radiative transfer models, which include only a disk wind, fail to reproduce blueshifted absorption for the interferometric system inclination (models detailed in Appendix B). Interestingly, we observe that as the wind absorption weakens, the [O I] emission strengthens. We suggest one possible physical interpretation for this anticorrelated EW evolution invoking star-disk interaction. Assuming the absorption is done by a compact wind originating near the star and that the observed [O I] emission originates in the disk surface layer, as the wind becomes less loaded with mass (weakening absorption), the emitting layer of the disk can remain low enough density that [O I] is able to spontaneously de-excite rather than being continually collisionally excited (thus strengthening emission). At velocities of a few hundred km s^{-1}, wind material would take ∼half a day to travel ∼0.1 au, making this scenario consistent with our observations.

While we do see significant variability within a single night of our observations of V1295 Aql, unfortunately, our data do not cover a sufficiently long time baseline to establish whether there is any periodicity to the variability that could be attributed to rotational modulation (periodicity has been seen in CTTS, cf. Johns & Basri 1995, and references therein). We observe persis-

TABLE 2
STELLAR PARAMETERS

	V1295 Aql		HD 98922	
Spectral type	A2e		B9e	
T_{eff} [K]	9250±250	2	10600	3
Mass [$M_\odot$]	2.9±0.5	4	5	5
Radius [$R_\odot$]	3.6±0.5	4	9.1	3
Inclination [°]	34±2	6	20-45	7, 8
v_r [km s^{-1}]	-1.2±1.3	1	-4.9±4.4	1
$v\sin i$ [km s^{-1}]	3.2±2.5	1	39±5.3	1
P_{rot} [d]	32±25	1	4-8	1
Magnetic field strength [G]	∼100	9, 4, 10, 11	Non detection	11

NOTE. — References: 1. Derived in this work with MIKE spectra, rotation periods calculated as P= $2\pi R_{star}\sin i$ / $v\sin i$. Errors cited incorporate the error on radius, $v\sin i$, and i; V1295 Aql's uncertainty is dominated by uncertainty on $v\sin i$; a range is given for HD 98922, as a large range of inclination values are reported in the literature. 2. Acke & Waelkens (2004), using spectral type and best visually-matched synthetic spectrum; 3. Kraus et al. (2008b), R calculated using T_{eff} and L; 4. Catala et al. (2007), <B> from spectropolarimetry and mass, radius, from PMS track placement; 5. Wade et al. (2007), masses, radii derived via PMS track placement; 6. Lazareff et al. (2017), H-band interferometry assuming shared star and disk inclination; 7. Hales et al. (2014), inclination from combined ^{12}CO and SED modeling; 8. Blondel & Djie (2006), inclination from fitting shape of Lyman-α profile; <B> from spectropolarimetry in 9. Hubrig et al. (2006), 10. Hubrig et al. (2009), and 11. Alecian et al. (2013c).

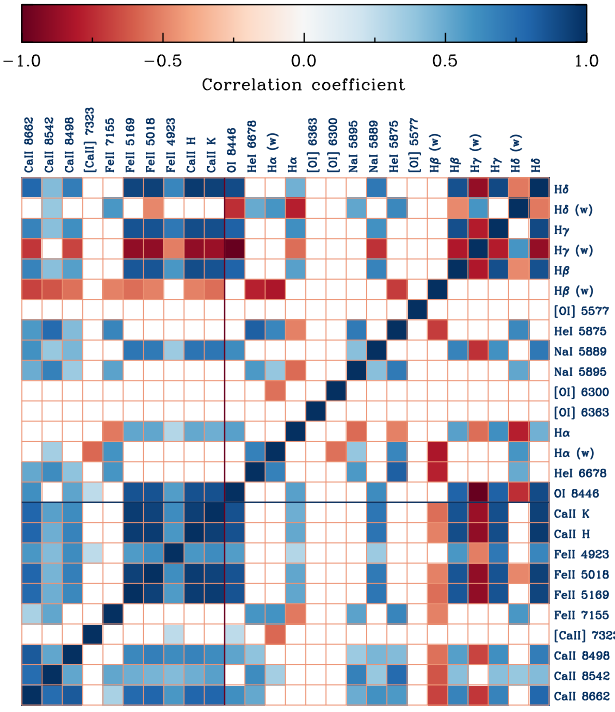

FIG. 3.— Correlations of time-series line EWs for V1295 Aql, 2013 high cadence spectra only were used here. Lines are grouped by ionization state (singly ionized the left and below dividing lines, neutral to the right of and above) and within those groups, sorted by increasing excitation energy to the upper right corner.

tent, weak absorption and emission components within the blueshifted absorption in Hα, not attributable to any telluric features, and have used a local minimum and maximum finding algorithm to quantify their velocities and evolution during the observation window (see Appendix C). We find that the lower velocity structures (between ∼-190 to -234 km s^{-1}) remain stationary while the higher velocity structures (≤-265 km s^{-1}) accelerate. The highest velocity transient absorption feature both accelerates and decelerates during our observation window; potentially, given the short timescale of significant velocity evolution, we are observing structures entrained and corotating in a stellar wind.

4.2. *HD 98922*

HD 98922 is a B9e star between 20-45° inclination (Blondel & Djie 2006; Hales et al. 2014); it has no detected magnetic field (Alecian et al. 2013c). From our MIKE spectra, we measure $v\sin i$ to be 38.9±5.31 km s^{-1}, and the V_r is −4.88±4.43 km s^{-1}. Varying the inclination within the reported range of values from the literature, we obtain rotation periods between 4-8 days; thus our observations likely span a full rotation period. We see the greatest variability on the order of day to year timescales, however, substantial variability is observed over the course of our observations in 2013 (Fig. 2, left panel). The shorter timescales are most consistent with rotational modulation, but we do not detect periodicity on ∼day timescales in either object.

In Figure 4 we show the EW(t) correlation matrix as described in Section 4.1. We see strong anticorrelation of the evolution of Na I D line widths and the higher order Balmer series lines, including both emission and absorption components; in contrast, the Na I D line width evolution is weakly correlated with Hβ and any correlation or anticorrelation with Hα is not statistically significant. Anticorrelation would not be expected in the TTS case, where Hα and Na I D emission have been linked to an accretion flow (e.g., the models of Muzerolle et al. 2004), but it is unclear what differing levels of correlation with different Balmer series lines could be indicating. In contrast to the same figure for V1295 Aql, we see more strongly related line profile evolution in HD 98922 generally, possibly simply due to our observations sampling a full rotation period. Despite the coverage, we searched for periodicity to line profile evolution and did not find any (we show our equivalent width time series measurements in Appendix A).

The wind, as probed through the line minimum in the Hα P Cygni component appears to be getting faster over

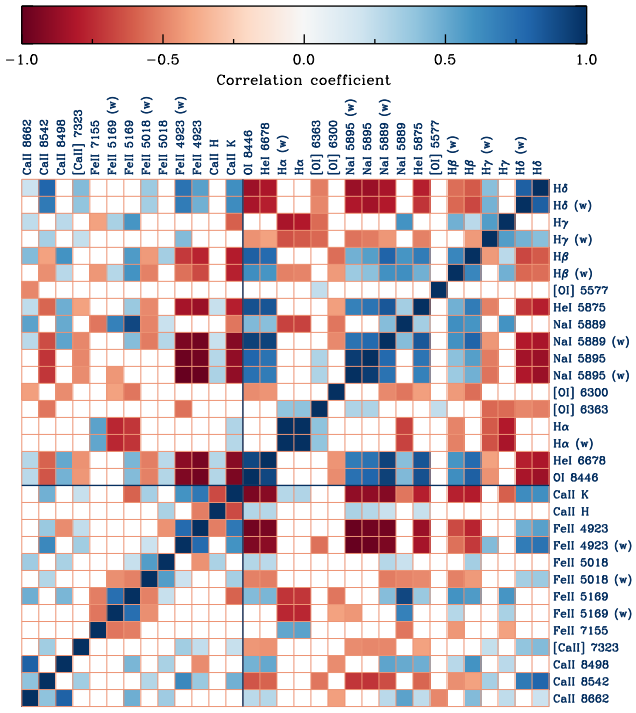

FIG. 4.— Correlations of time-series line EWs for HD 98922.

the course of observation. We note, however, the difficulty in modeling the wind as our high-resolution data allow us to see at least three distinct velocity minima in the P Cygni profile. Similar to the distinct weak absorption features in V1295 Aql, the lower velocity components (∼-50 to -100 km s^{-1}) in HD 98922 are static during our observations while the higher velocity components (∼-125 to -175 km s^{-1}) accelerate. When the velocity of the component doing the strongest absorbing is slow, during our 2013 MIKE observations, we see P Cygni absorption in the Na D lines; in the earlier epoch of MIKE data from 2010, when the wind is a factor of 2 faster (Fig. 1, upper left panel), there is no blueshifted absorption in the Na D lines. This is potentially probing mass loading in a wind and corresponding changes in the density gradient in the acceleration region: when the wind is slower, the density gradient is steeper toward the base of the launch region, causing the observed absorption in Na I. Powell et al. (2012) noted this in FU Ori, observing a 1.8d lag in variability between Na I and the blueshifted absorption in Hα; unfortunately, we lack temporal coverage in the earlier epoch of V1295 Aql data to search for a similar effect.

5. DISCUSSION

We have conducted a high cadence, time-series survey of two Herbig Ae/Be stars. Combining these new data with earlier observations by our team and archival spectra, we find strong variability in spectral line profiles on the longer timescales sampled: years, months, and days. We see very weak modulation on the shortest timescales sampled, ∼minutes. In all timescales, the strongest variability occurs in the blueshifted absorption components of the spectral lines. The lack of strong variability in lines' emission components as well as an absence of inverse P Cygni profiles is in distinct discord with our modeling efforts based on a dipolar magnetospheric accretion geometry. Given the lack of magnetic field detections in Herbig Ae/Be stars as well as the evidence for higher-order moments dominating global magnetic field structure as stellar mass increases (Gregory et al. 2012), the observed accretion in both systems may be taking place via higher-order magnetic field structure, a boundary layer, or at a novel magnetospheric inclination with respect to the rotation axis (i.e., misaligned).

In the case of V1295 Aql, the system inclination and variability on shorter than inner disk Keplerian timescales point to a stellar or X-wind originating close to the star, not a farther-out disk wind, as playing a role in generating the observed spectral lines. Catala et al. (2007) suggest the acceleration region at the base of a stellar wind as the origin of narrow metallic emission lines. Our magnetospheric accretion+disk wind model and the stellar wind model of Catala et al. (2007) demonstrate that a compact stellar wind acceleration region and a magnetosphere can produce the same emission profile; difficulty arises in how the blueshifted absorption is produced. Interferometric evidence for low system inclination makes it highly unusual that we observe as much variability in the blueward absorption components; indeed, our disk wind model cannot reproduce the observed absorption at such low system inclination. Observations by Alecian et al. (2013a) during overlapping epochs indicate the structure of the stellar magnetic field itself has changed, lending further support to material closer to the star being responsible for variations in line morphology. Potentially further evidencing a stellar wind, we observe anticorrelated evolution of the blueshifted absorption in Hα and [O I] 6300Å emission (i.e., as the Hα blueshifted absorption weakens, the [O I] emission strengthens) that may indicate a decrease in outflow sufficiently lowers the density in upper disk layers to enhance forbidden line emission; correlation is not seen when comparing the emission component of Hα to [O I]. Further, the Fe II (42) emission line, suggested by Catala et al. (2007) to be forming in a stellar wind, has positively correlated evolution with the emission components of all Balmer series lines. Lastly, the velocity structure of the blueshifted absorption in Hα is consistent with obscuring material moving at or faster than stellar escape velocity.

Our observations span the full rotation period of HD 98922; over this timescale, one may observe accretion flows moving in and out of the line of sight, modulating observed flux in spectral lines. We do observe strong variability in line profiles over this time, but do not find periodicity in the evolution of line equivalent widths. As in the case of V1295 Aql, the lack of any inverse P Cygni profile or variability on that side of the line, despite our full sampling of the stellar rotation period, is problematic for a canonical magnetospheric accretion paradigm. Unlike V1295 Aql, HD 98922 is at an intermediate inclination and the blueshifted absorption can be readily reproduced via disk wind. We see anticorrelation of the Na I D lines' evolution and Hδ and Hγ, but weak correlation with Hβ and no significant correlation with Hα; the significance of this is unclear, but positive correlation would be expected were all the lines to originate in an accretion flow.

Models of disk winds have recently begun to take into

account the disk magnetic field. Of particular import to the HAeBe case, the models of Bai & Stone (2013) show that in the presence of a strong FUV field, the wind mass loss rate is boosted; an FUV flux increase of an order of magnitude increases the mass loss rate by a factor of 3. In developing a picture of accretion and outflow for intermediate to higher mass protostars, the winds–both stellar and disk in origin–will likely be critical to understand, playing a dominant role in the system mass flux.

For the two systems studied here, it is another interesting point of contrast that in one case, the time evolution of emission and absorption components in the same line profile are apparently unrelated (V1295 Aql) while in the other, they are strongly correlated (HD 98922). Broadly, the differing evolution of lines in the same multiplet or series that would be expected to co-evolve underscore the need for rigorous definitions of line components due to the potential for overlapping temporal and spatial properties. The ambiguity of line profiles, e.g., the degeneracy in emission line production by an extended magnetosphere versus a pure P-Cygni spherical wind (i.e., our modeling of the Hα line of V1295 Aql) calls for more rigorous, multi-component models that include asymmetry. High resolution, high cadence spectroscopy reveals spectral line structure on fine velocity/spatial and temporal scales while $\sim$nightly visits and multi-epoch data demonstrate rotational and longer-term system evolution, both of which are necessary to inform models of evolving modes of accretion and outflow with increasing stellar mass.

A. N. A. would like to acknowledge the support of NASA Origins of Solar Systems grant NNX09AB87G to J. D. M. and NSF AAG F034342 to A. N. A. and J. D. M. The authors thank B. P. Brown for computational contributions; models were calculated with support of the NASA High End Computing (HEC) Program through the NASA Advanced Supercomputing (NAS) Division at Ames Research Center on Pleiades with allocation GID s1647. S. K. acknowledges support from a STFC Rutherford fellowship (ST/J004030/1) and ERC Starting Grant (Grant Agreement No. 639889). We also express appreciation for observations taken for this program by Ajay Tannirkulam, Xiao Che, Stefan Kraus, Mario Mateo, Keren Sharon and Traci Johnson. Finally, the authors thank an anonymous referee for thorough comment and suggestions that improved the manuscript.

APPENDIX

A. SPECTRAL ATLAS

Here we show spectra of all species discussed in the text for V1295 Aql (Figs. 5- 26 and HD 98922 (Figs. 27-48). The figures are in order of appearance in the correlation matrices (Figs. 3 and 4): singly ionized species first and neutrals second, sorted in order of increasing excitation potential within those groups.

V1295 Aquila

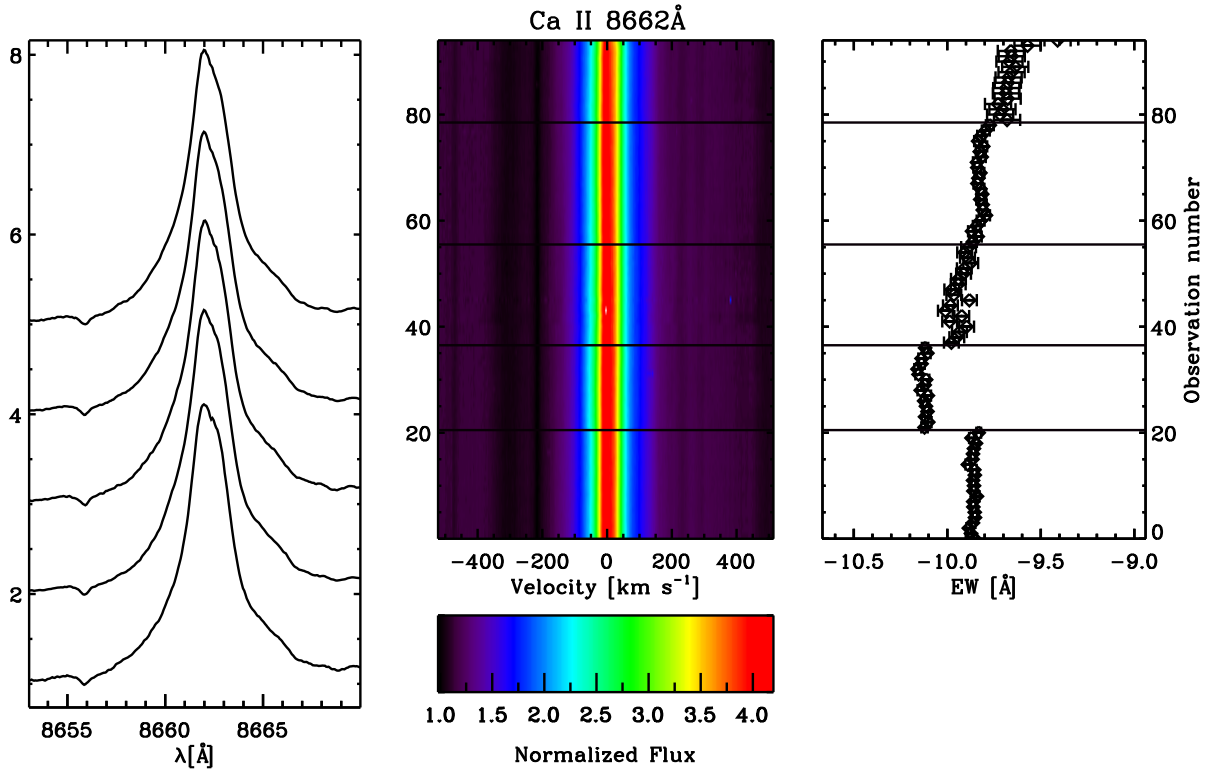

FIG. 5.— V1295 Aql Ca II 8662Å. Left panel: Average line profiles for each of the five nights of high cadence observation, increasing in time from bottom to top: UT130429, UT130503, UT130504, UT130506, UT130507. Spectra are continuum normalized, their photospheric components removed, and arbitrary y-axis offsets are applied for display purposes. Middle panel: surface plot showing every spectrum observed, ascending time order from bottom to top. Spectra are continuum normalized, their photospheric components removed, and a color scale is shown in bar below figure. Each night is separated by a horizontal line. Right panel: measured equivalent widths as a function of time. Unless otherwise indicated, total line equivalent widths are shown (including both emission and absorption components). Abscissa reversed to indicate decreasing emission line strength to the right. Error bars indicate RMS of measurements within a single night.

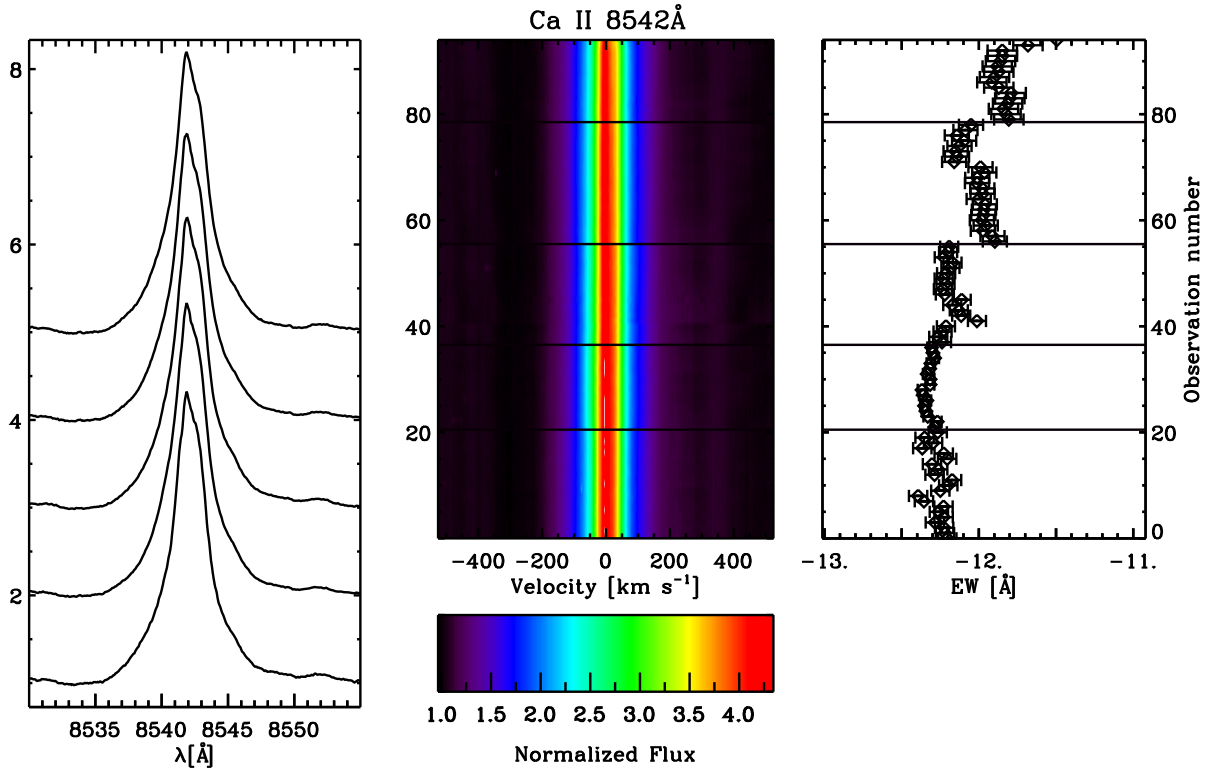

FIG. 6.— V1295 Aql Ca II 8542Å. As in Fig. 5.

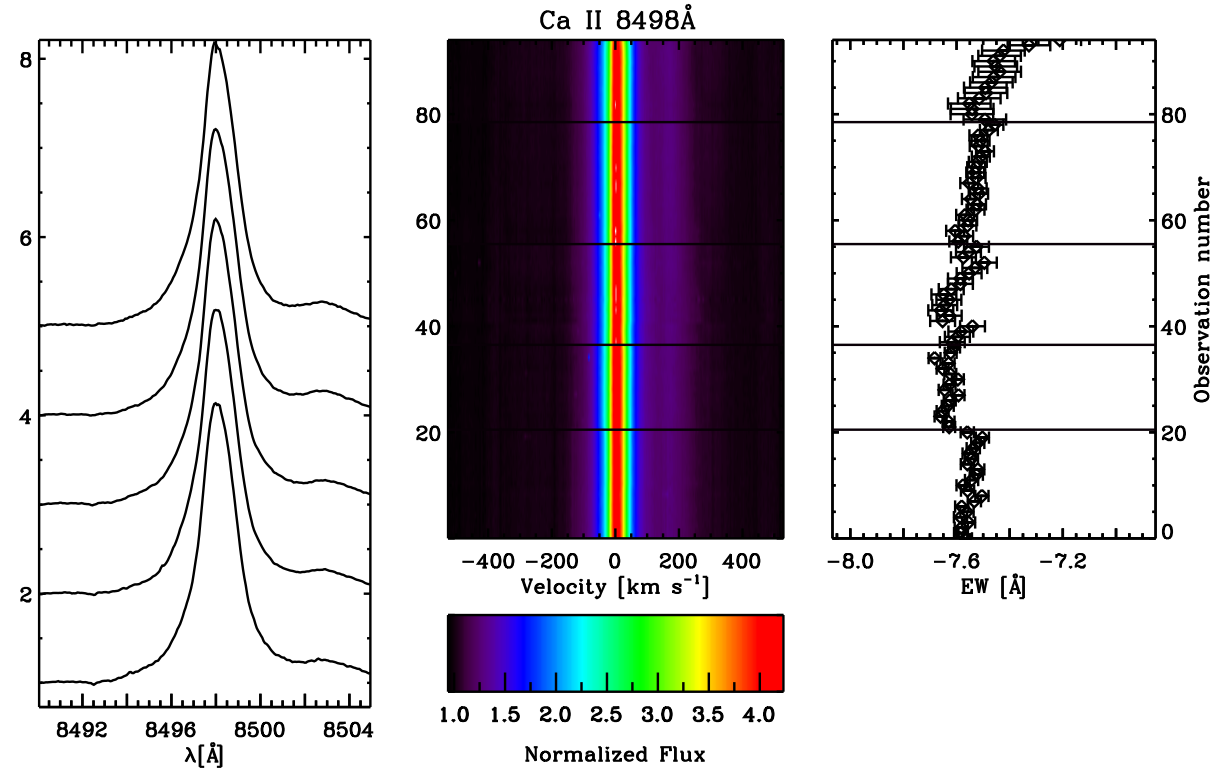

FIG. 7.— V1295 Aql Ca II 8498Å. As in Fig. 5.

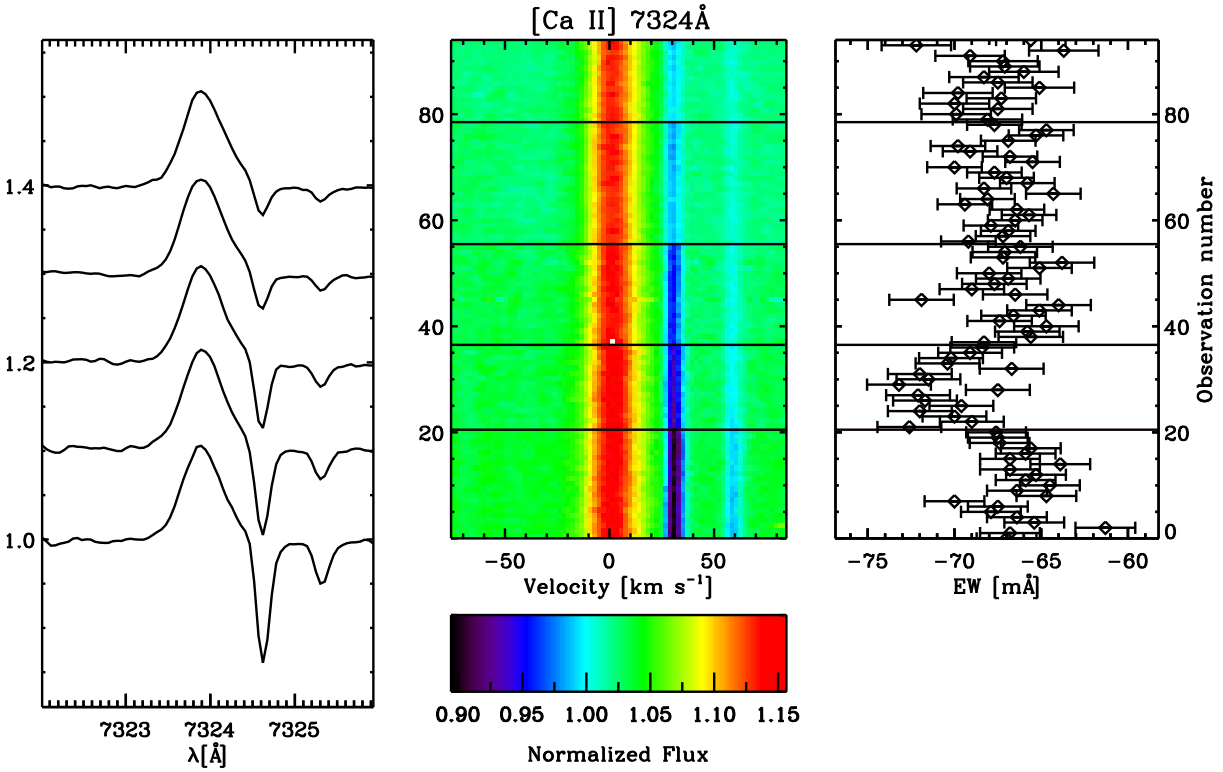

FIG. 8.— V1295 Aql [Ca II] 7324Å. As in Fig. 5. A telluric absorption line at 7324.14Å is overpowered here by the emission, but two water vapor lines are seen redward of the emission line (Kurucz 2005).

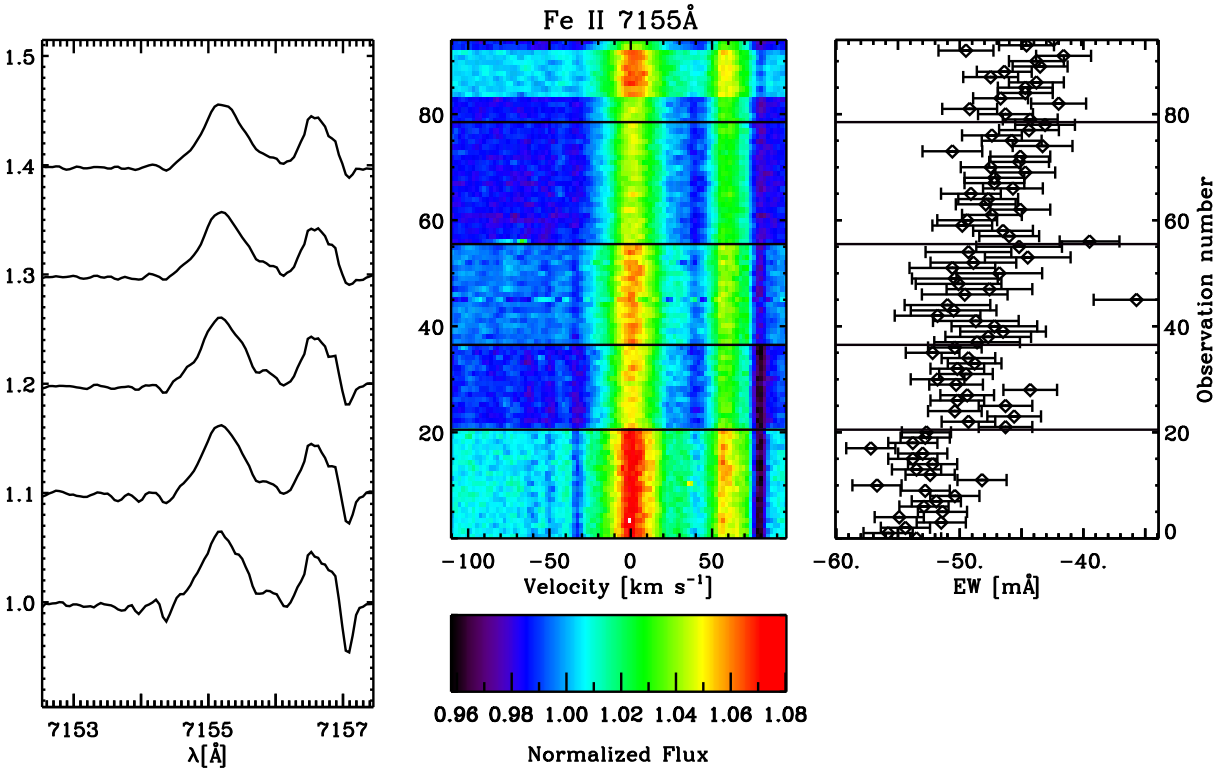

FIG. 9.— V1295 Aql Fe II 7155Å. As in Fig. 5. A telluric line at 7156.3Å is clearly seen to vary from night to night (Catanzaro 1997).

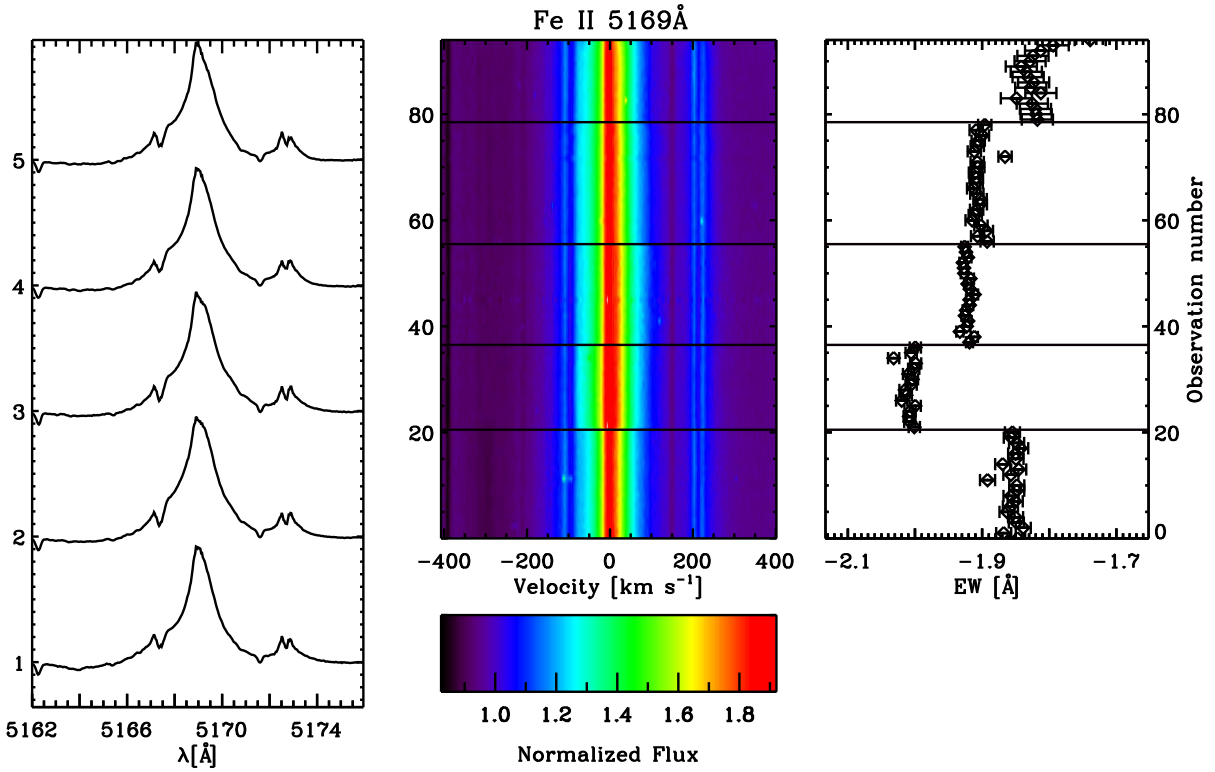

FIG. 10.— V1295 Aql Fe II 5169Å. As in Fig. 5.

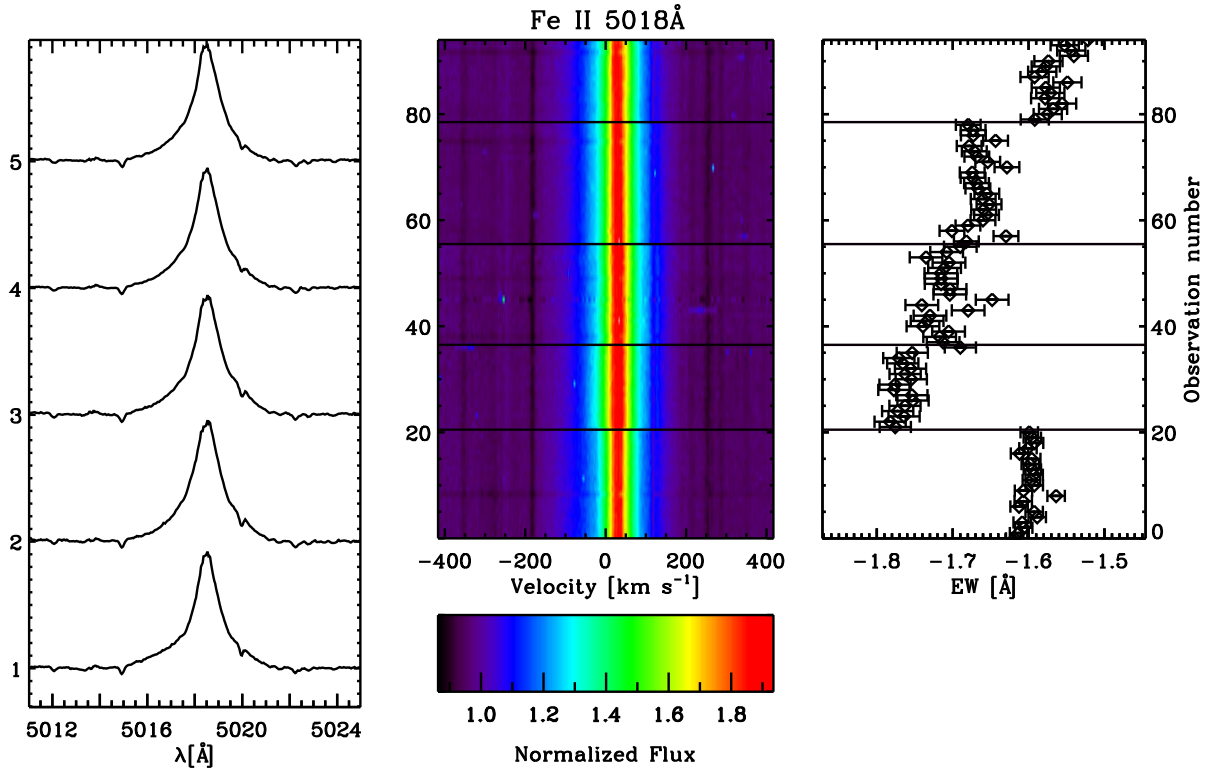

FIG. 11.— V1295 Aql Fe II 5018Å. As in Fig. 5.

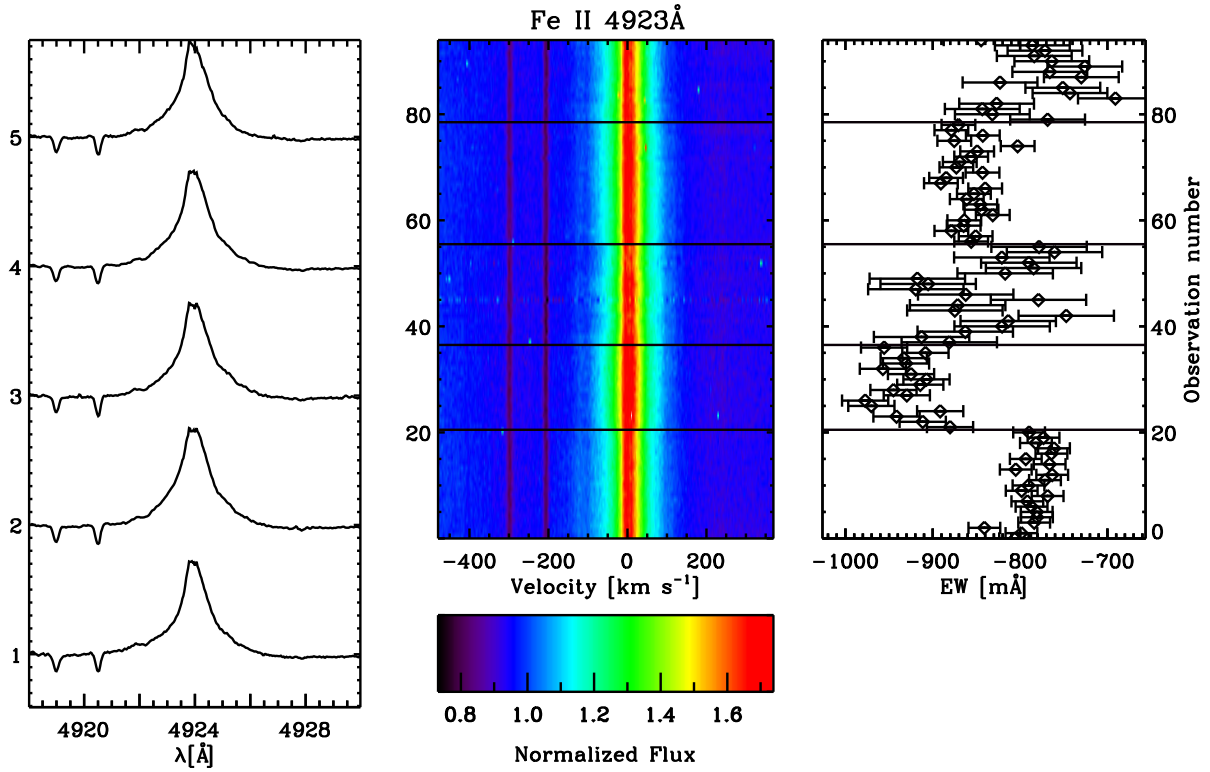

FIG. 12.— V1295 Aql Fe II 4923Å. As in Fig. 5. Poor seeing on the third night, as well as the line being on the edge of the MIKE red chip, contribute to the scatter in EW.

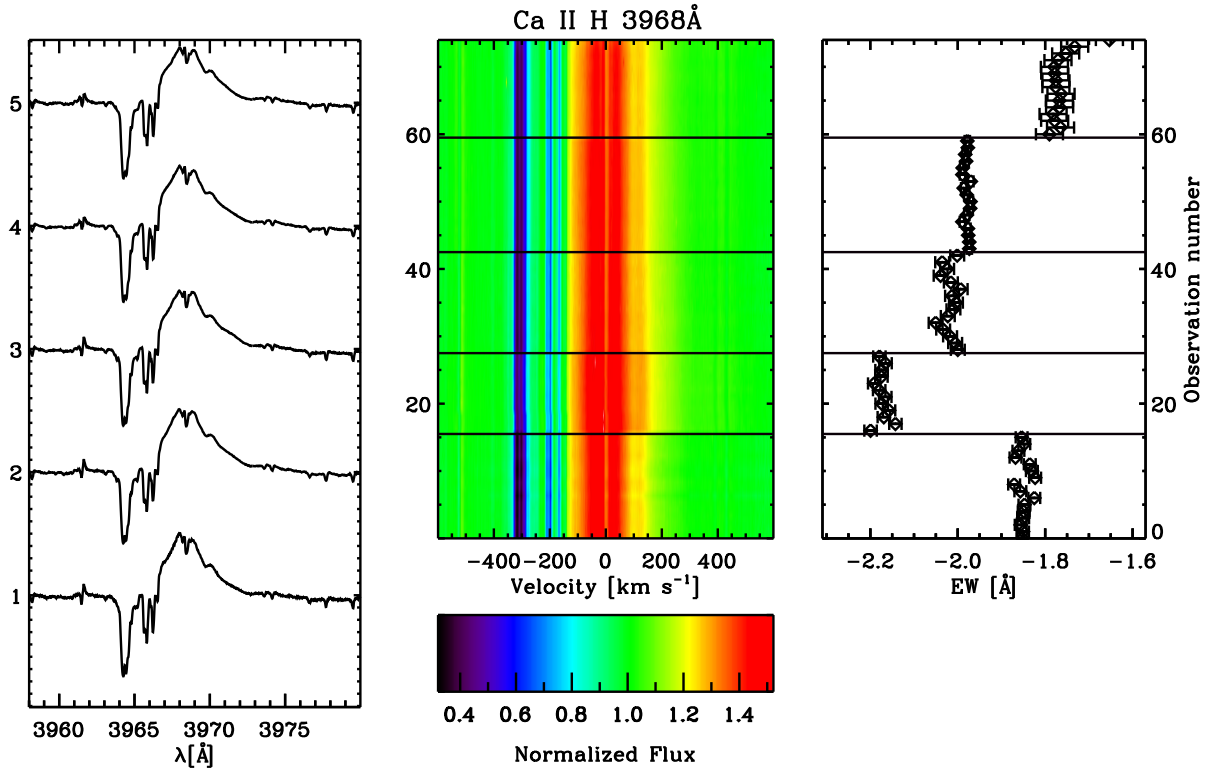

FIG. 13.— V1295 Aql Ca II 3968Å. As in Fig. 5.

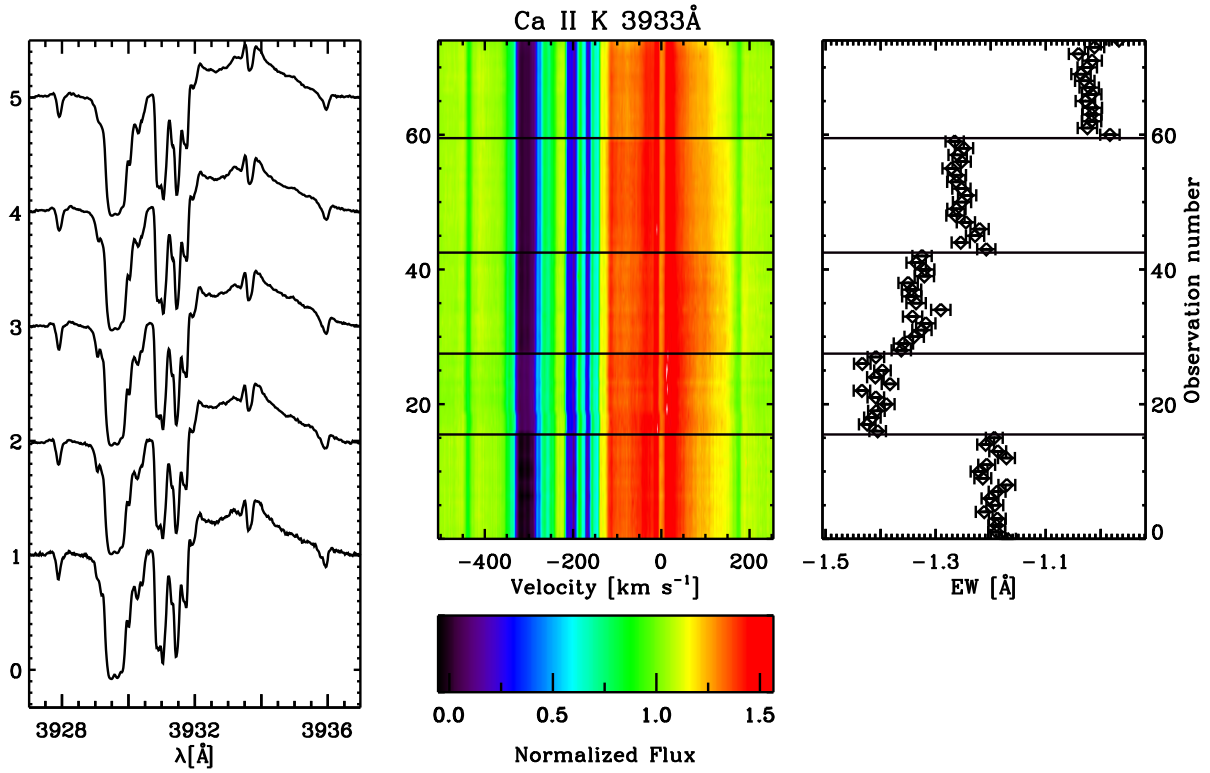

FIG. 14.— V1295 Aql Ca II 3933Å. As in Fig. 5.

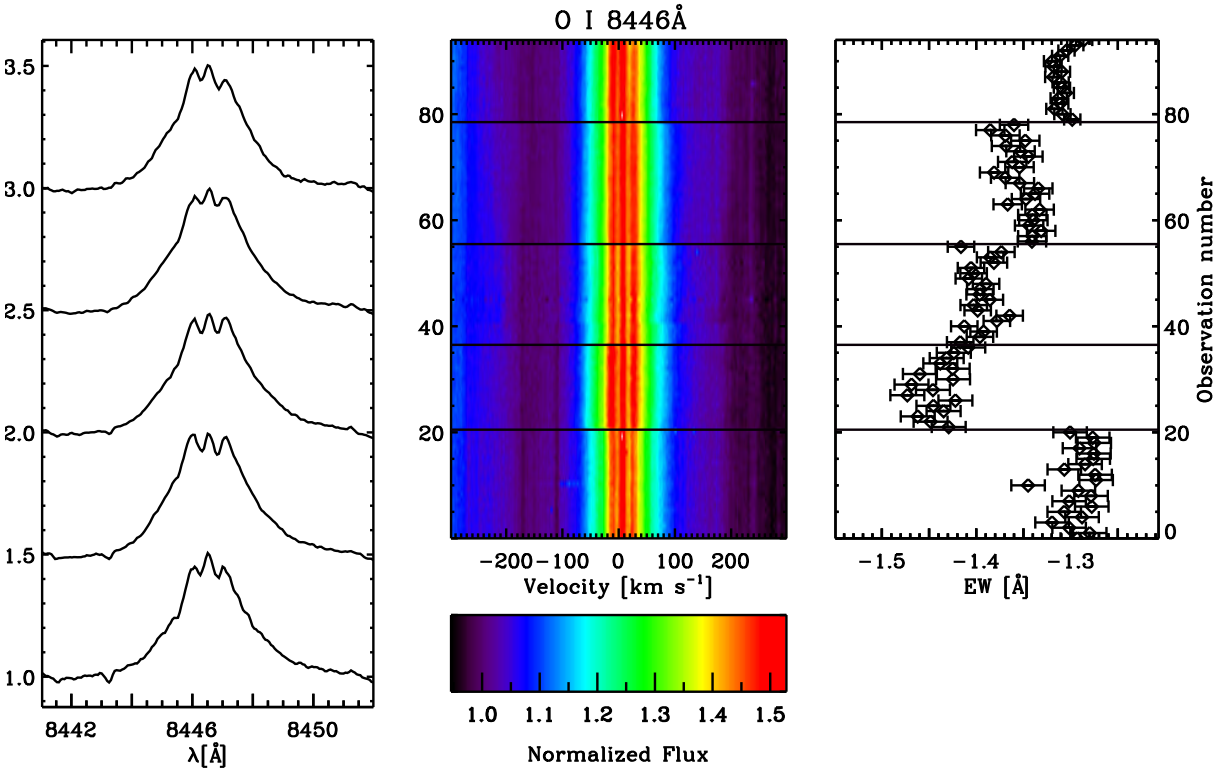

FIG. 15.— V1295 Aql O I 8446Å. As in Fig. 5.

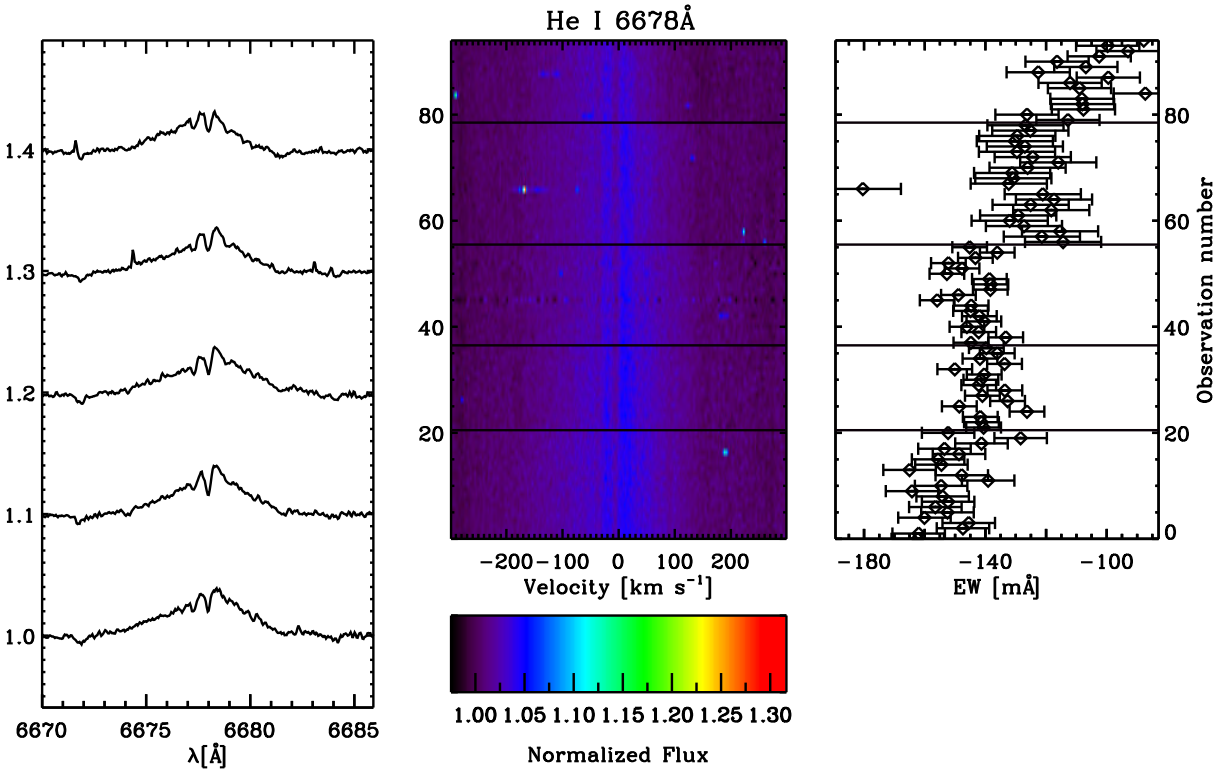

FIG. 16.— V1295 Aql He I 6678Å. As in Fig. 5.

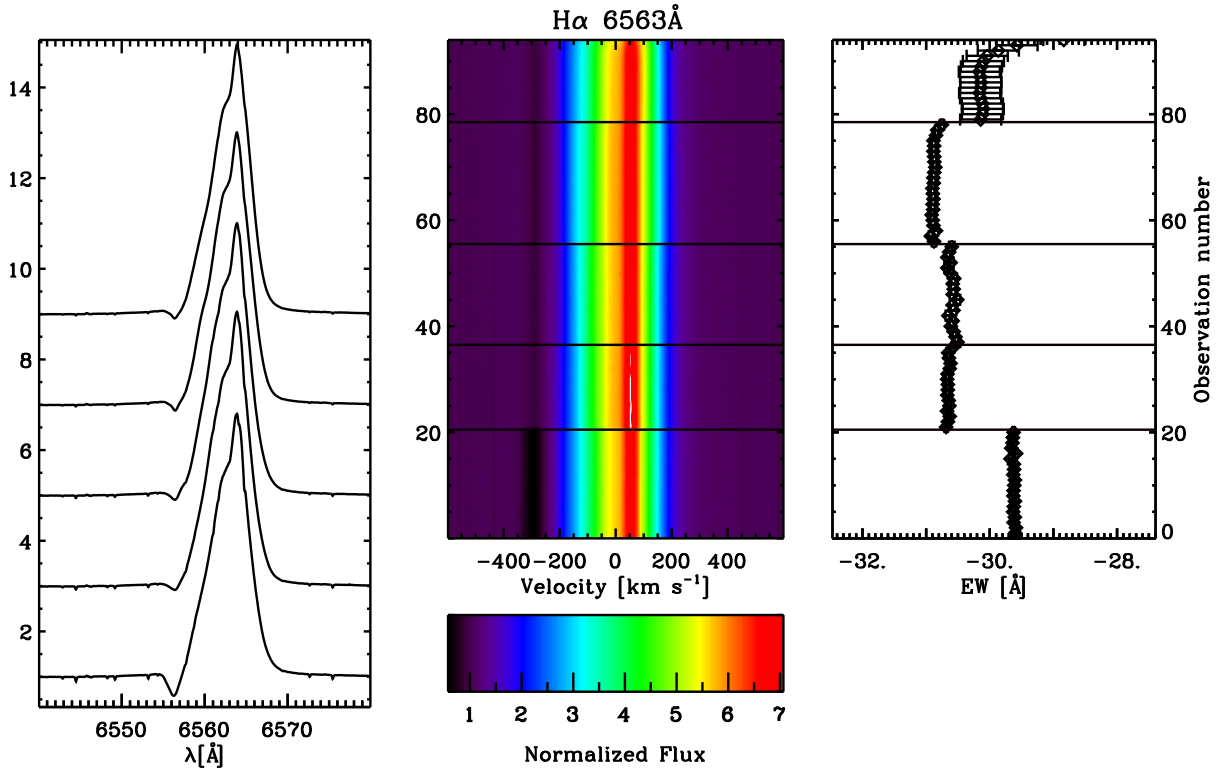

FIG. 17.— V1295 Aql Hα. As in Fig. 5. Here, we show just the fit emission components' EW for plot scaling purposes.

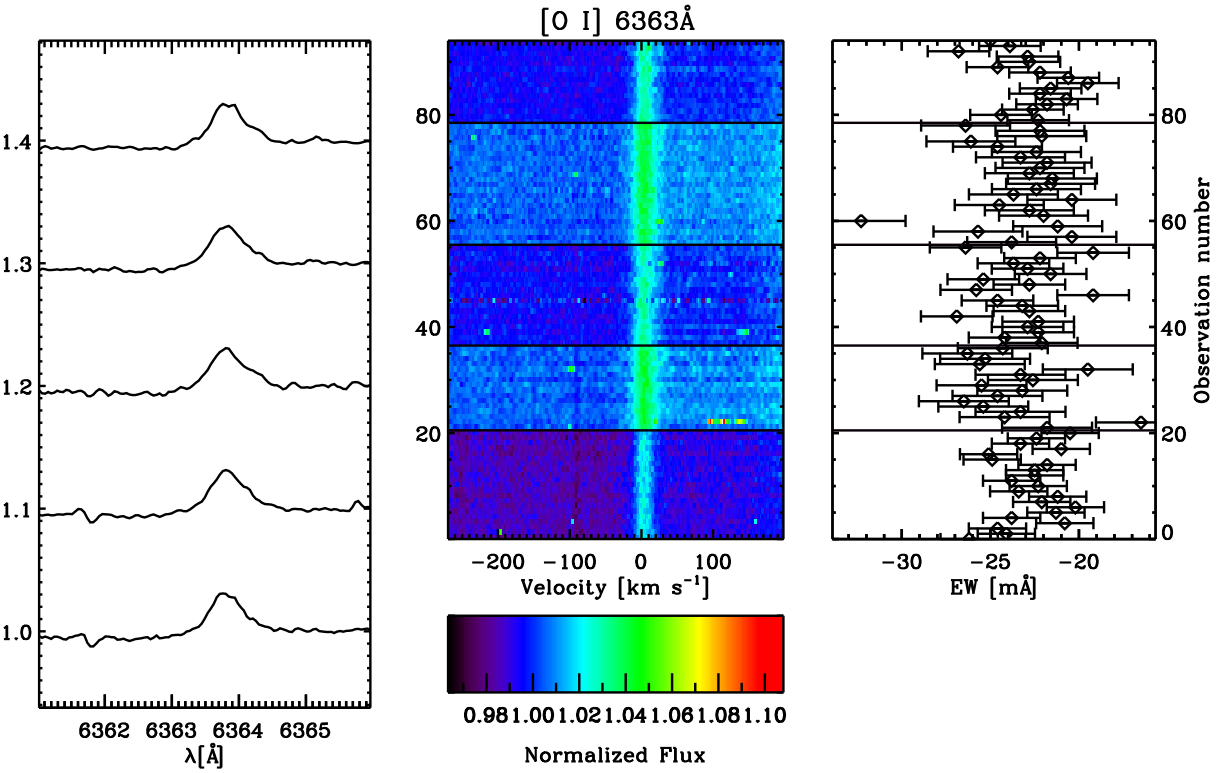

FIG. 18.— V1295 Aql [O I] 6363Å. As in Fig. 5.

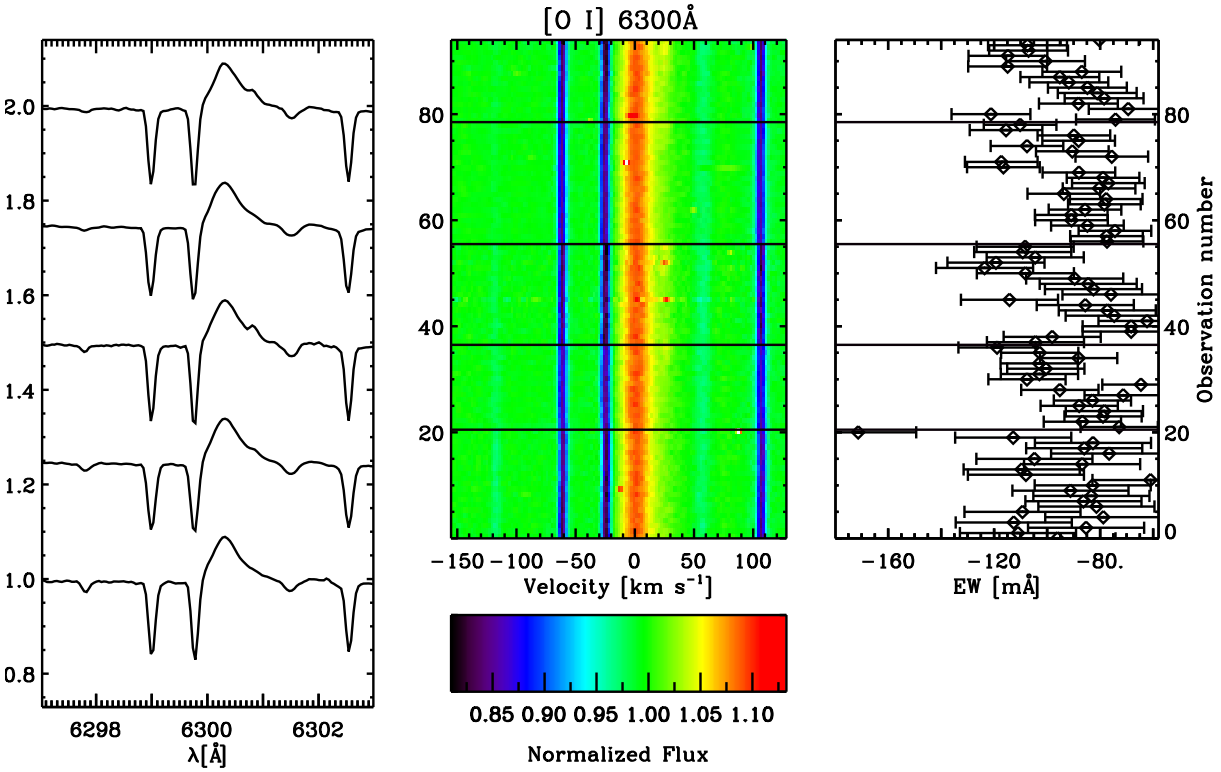

FIG. 19.— V1295 Aql [O I] 6300Å. As in Fig. 5.

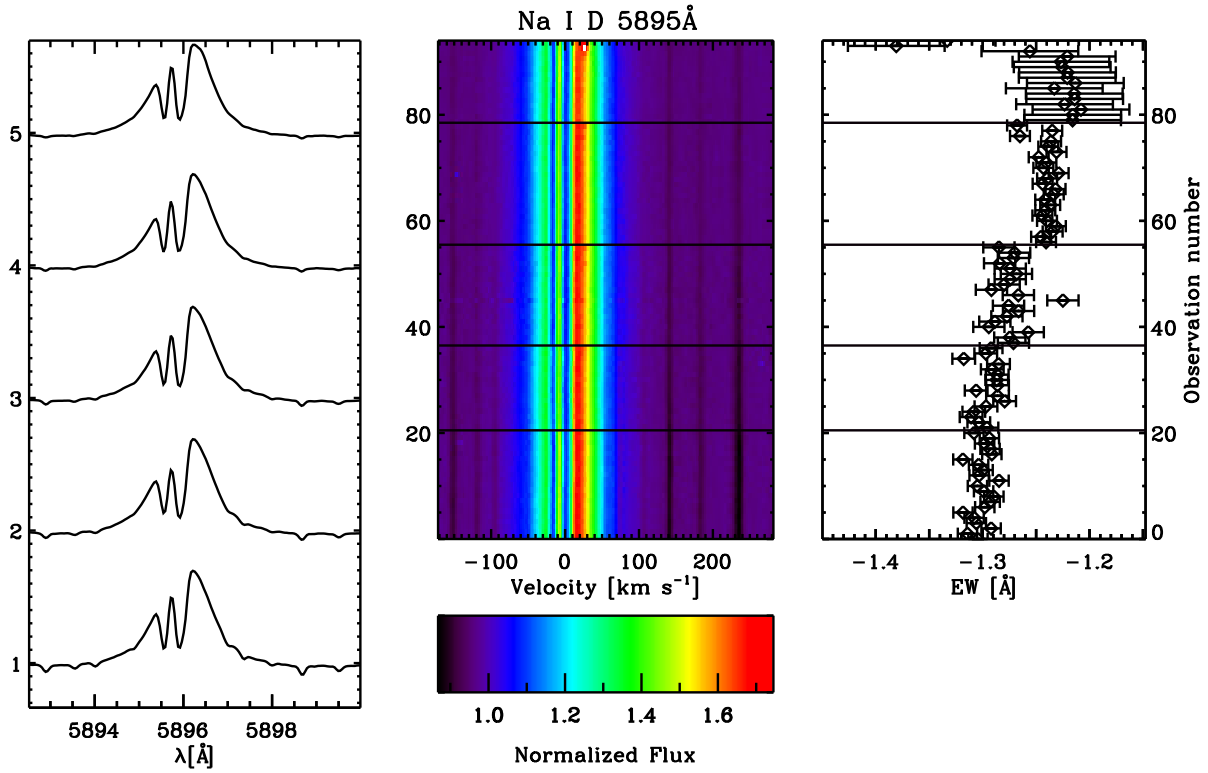

FIG. 20.— V1295 Aql Na I 5895Å. As in Fig. 5. Noise in the last few observations, visible as hot pixels in the surface plot, created the scatter in the last night's EW measurements. We saw this occur in both Na I D lines; its origin is unclear.

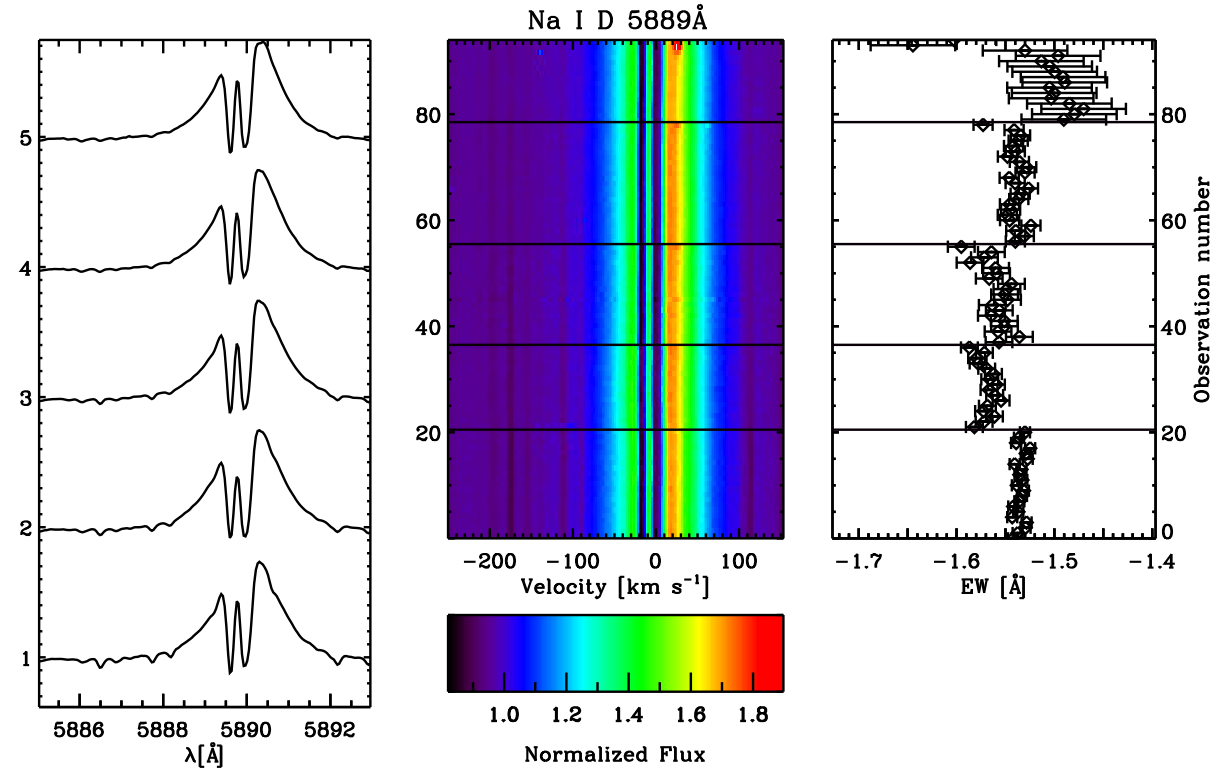

FIG. 21.— V1295 Aql Na I 5889Å. As in Fig. 5. Noise in the last few observations, visible as hot pixels in the surface plot, created the scatter in the last night's EW measurements. We saw this occur in both Na I D lines; its origin is unclear.

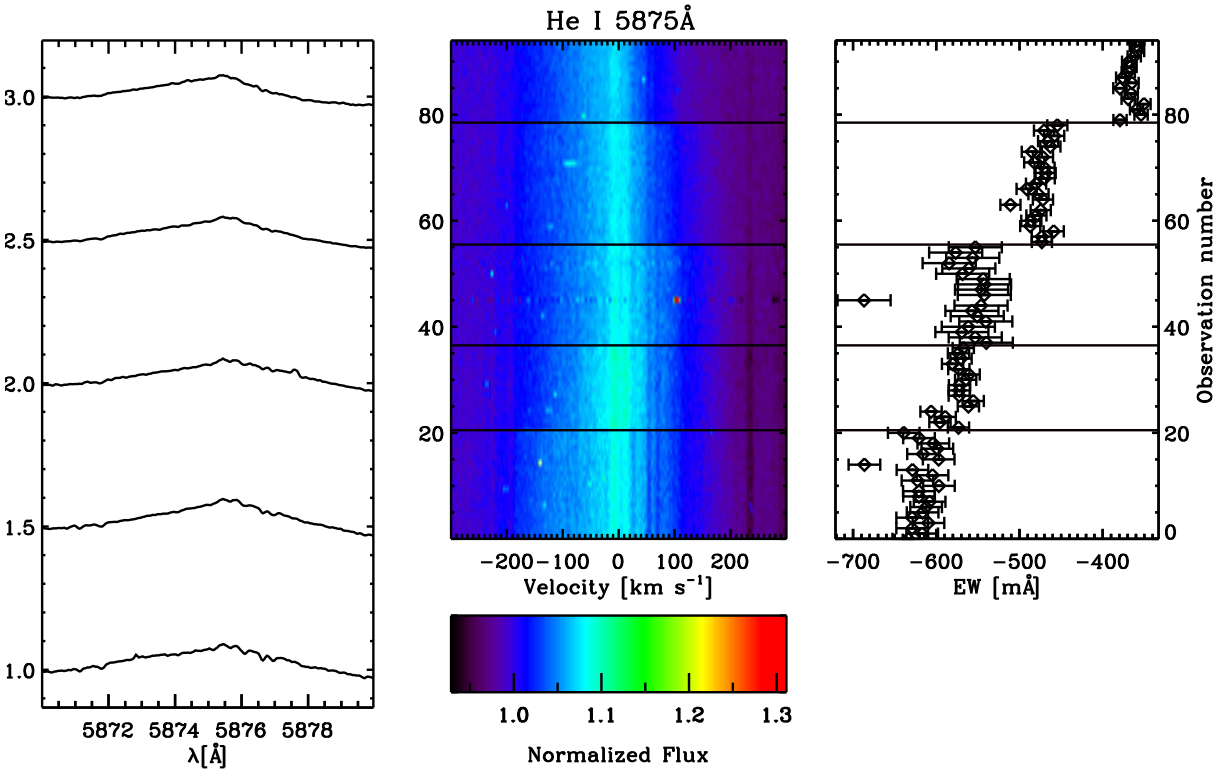

FIG. 22.— V1295 Aql He I 5875Å. As in Fig. 5.

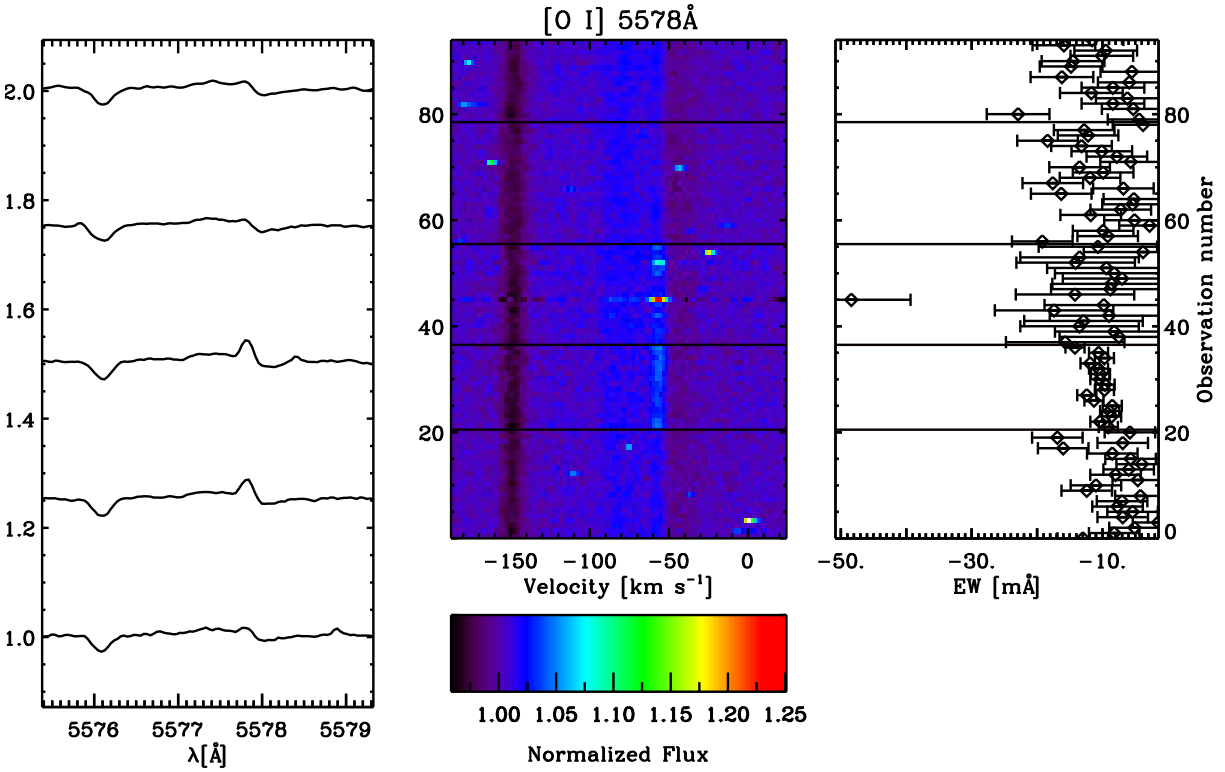

FIG. 23.— V1295 Aql O I 5578Å. As in Fig. 5. We suggest this line, due to its weakness and night to night variability (unlike other forbidden lines we observe which don't vary much), could simply be airglow (Louistisserand et al. 1987) and neither stellar nor circumstellar in origin.

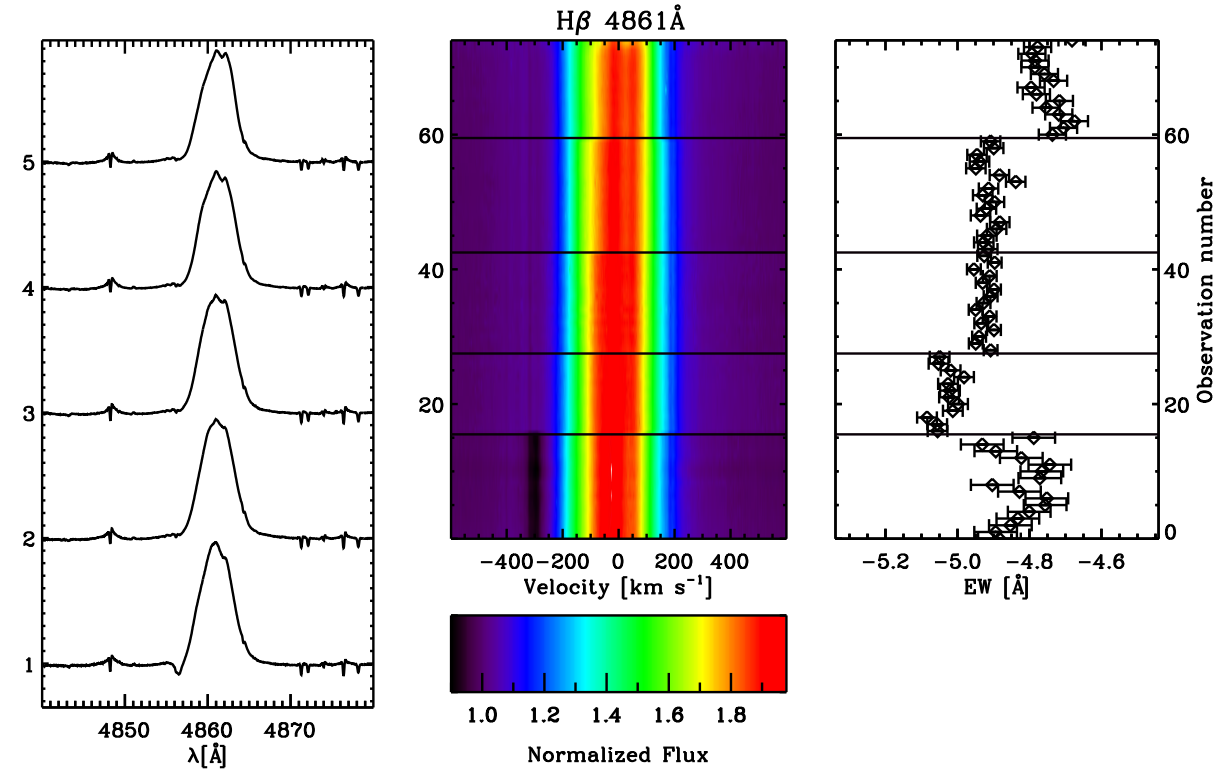

FIG. 24.— V1295 Aql Hβ. As in Fig. 5. Here, we show just the fit emission components' EW for plot scaling purposes.

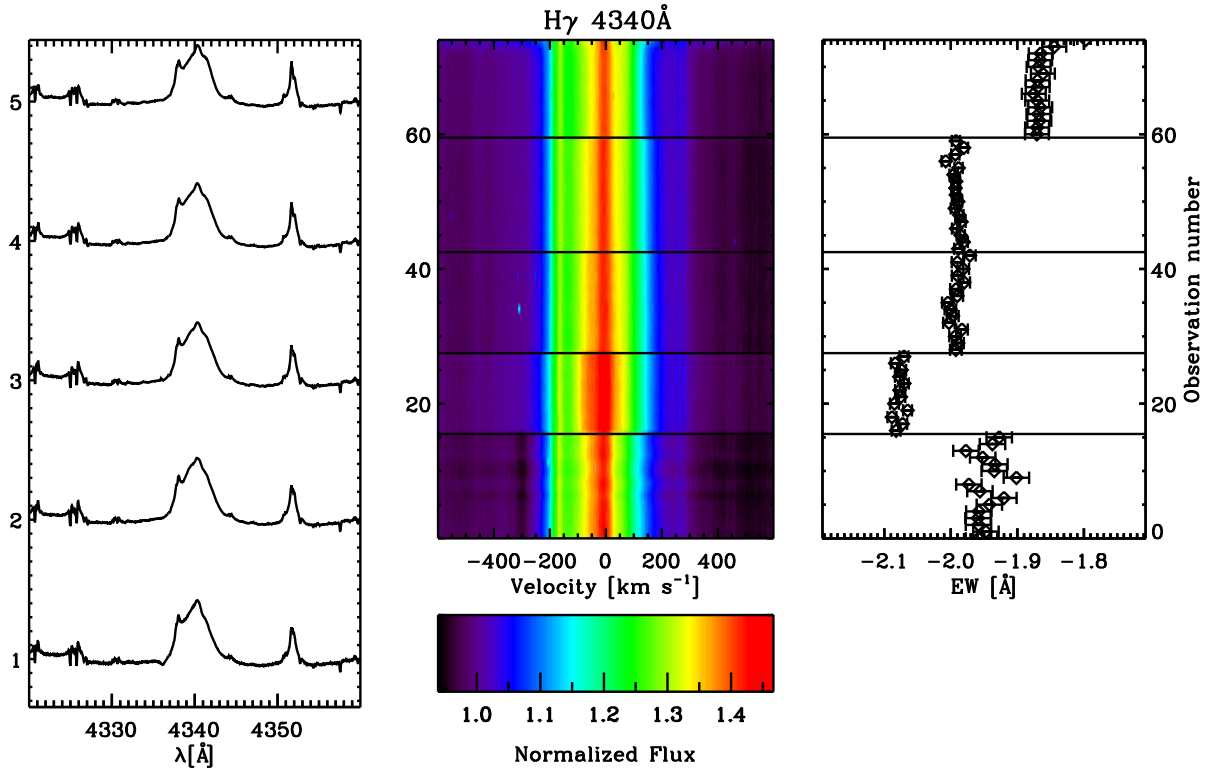

FIG. 25.— V1295 Aql Hγ. As in Fig. 5. Here, we show just the fit emission components' EW for plot scaling purposes.

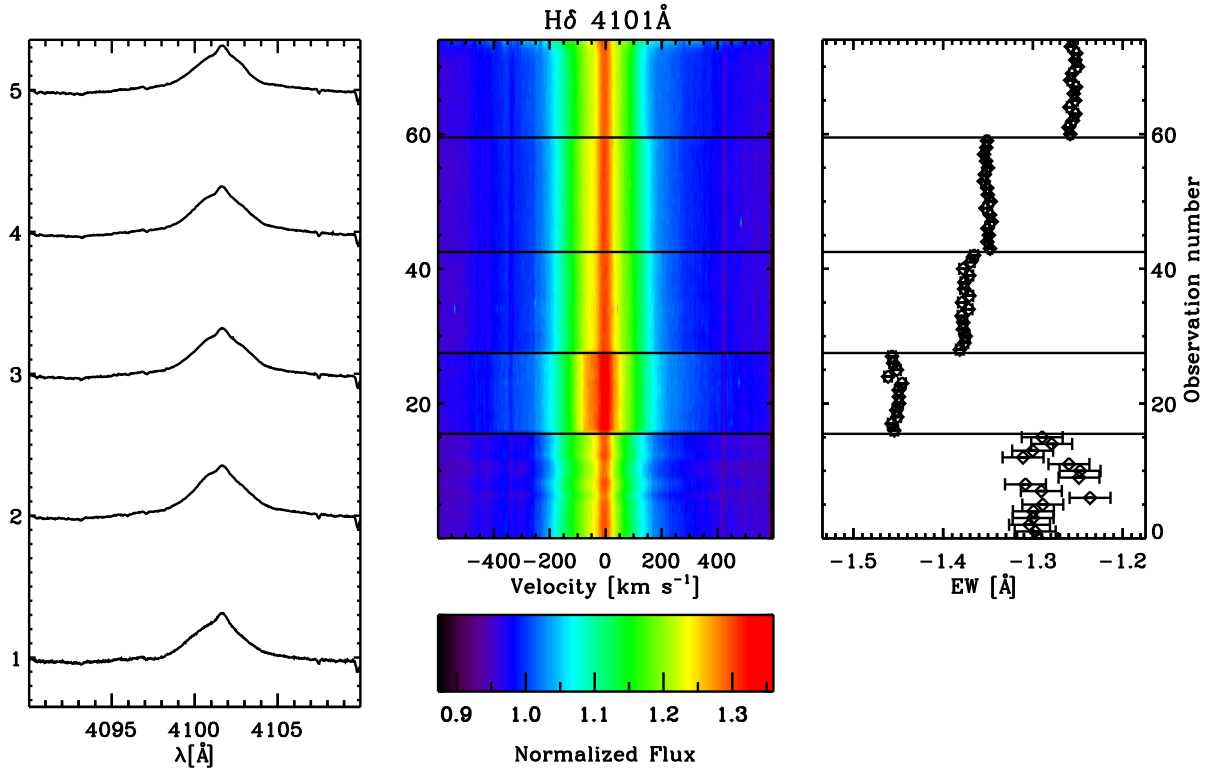

FIG. 26.— V1295 Aql Hδ. As in Fig. 5. Here, we show just the fit emission components' EW for plot scaling purposes.

HD 98922

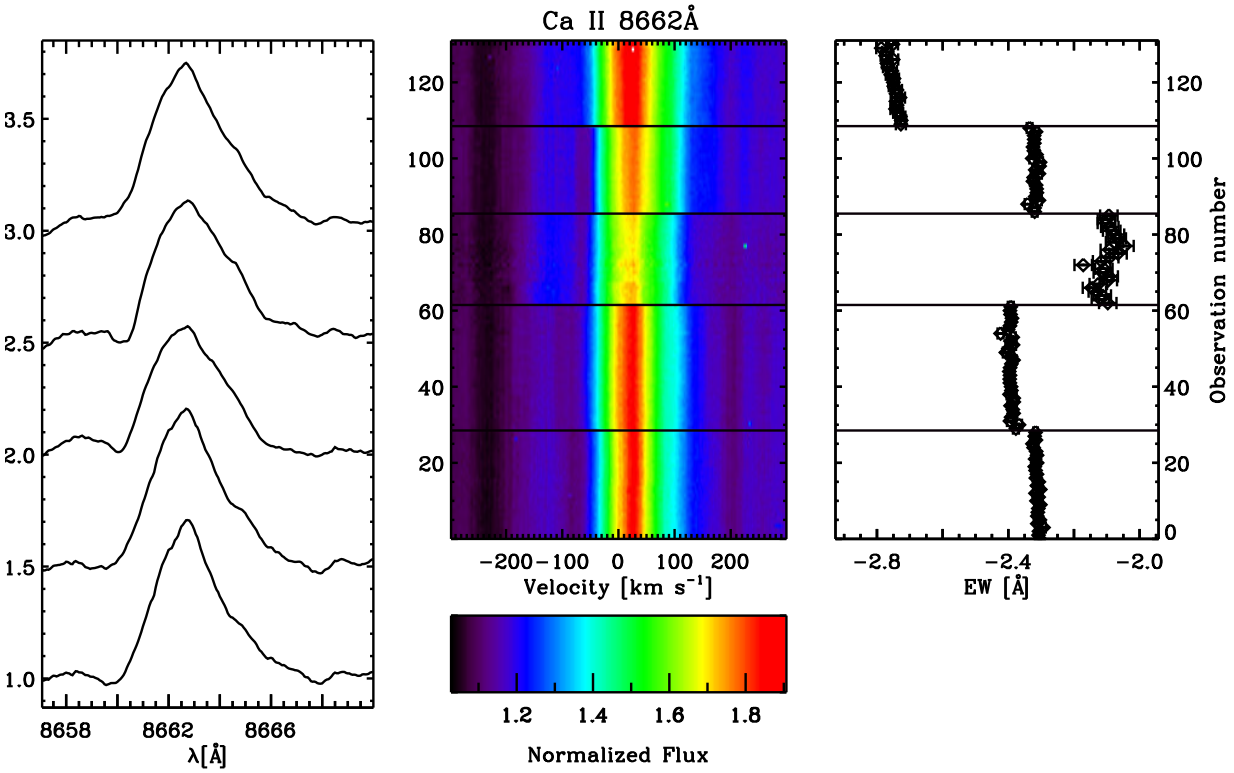

FIG. 27.— Left panel: Average line profiles for each of the five nights of high cadence observation, increasing in time from bottom to top: UT130428, UT130429, UT130503, UT130504, UT130506. Spectra are continuum normalized, their photospheric components removed, and arbitrary y-axis offsets are applied for display purposes. Middle panel: surface plot showing every spectrum observed, ascending time order from bottom to top. Spectra are continuum normalized, their photospheric components removed, and a color scale is shown in bar below figure. Each night is separated by a horizontal line. Right panel: measured equivalent widths as a function of time. Unless otherwise indicated, total line equivalent widths are shown (including both emission and absorption components). Abscissa reversed to indicate decreasing emission line strength to the right. Error bars indicate RMS of measurements within a single night.

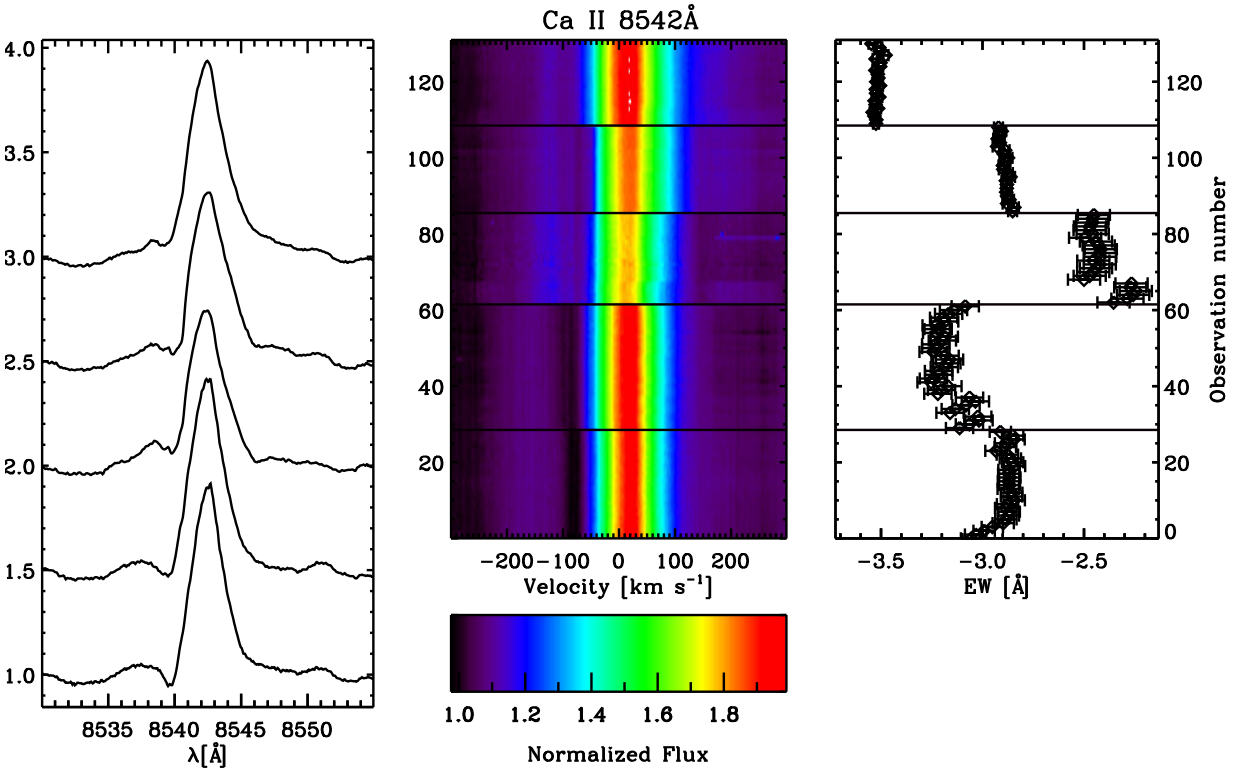

FIG. 28.— HD 98922 Ca II 8542Å. As in Fig. 27.

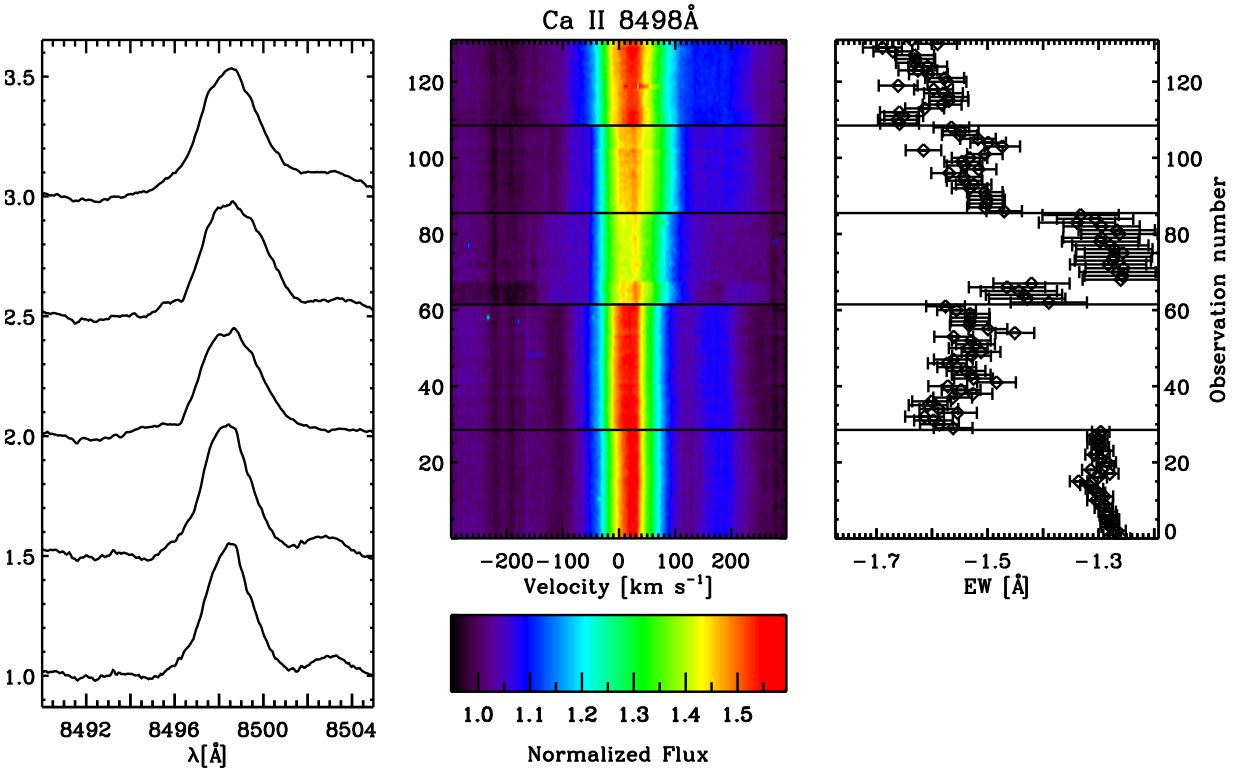

FIG. 29.— HD 98922 Ca II 8498Å. As in Fig. 27.

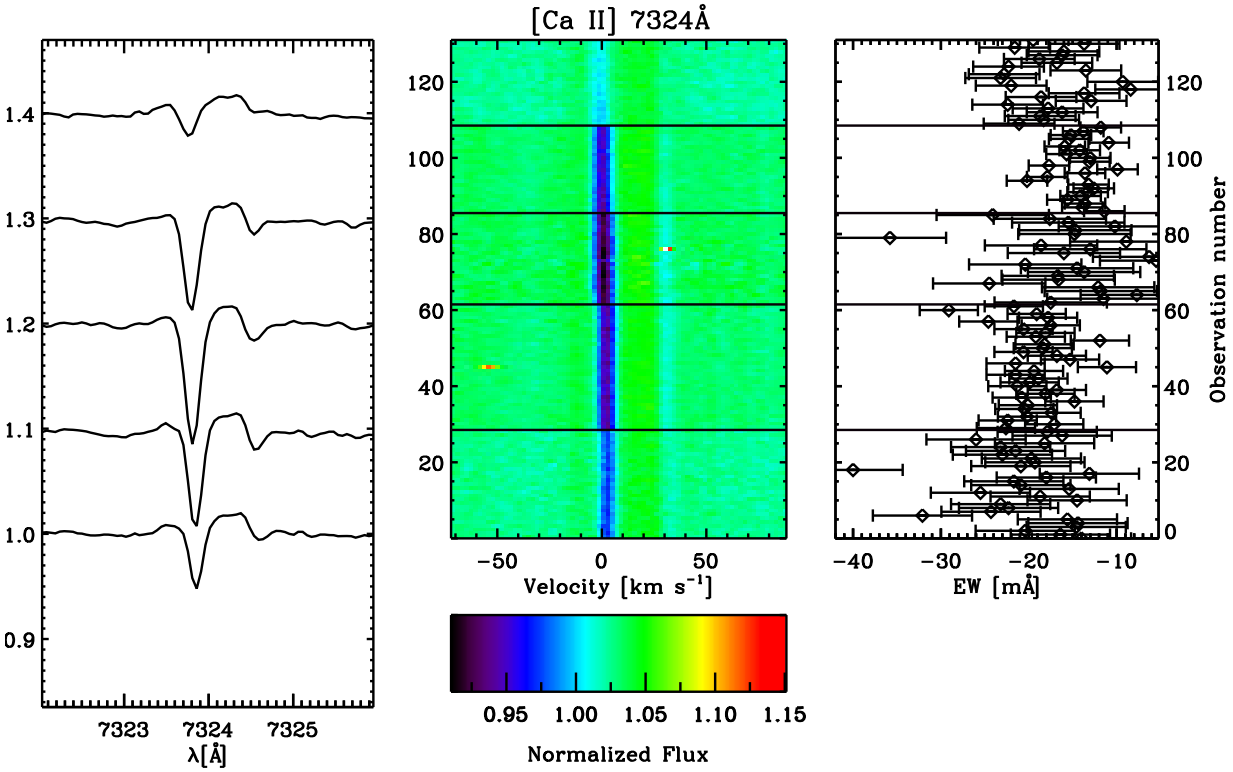

FIG. 30.— HD 98922 [Ca II] 7324Å. As in Fig. 27. Two water vapor lines are seen superimposed on the line and redward of it (Kurucz 2005). Here we show only the emission component EW.

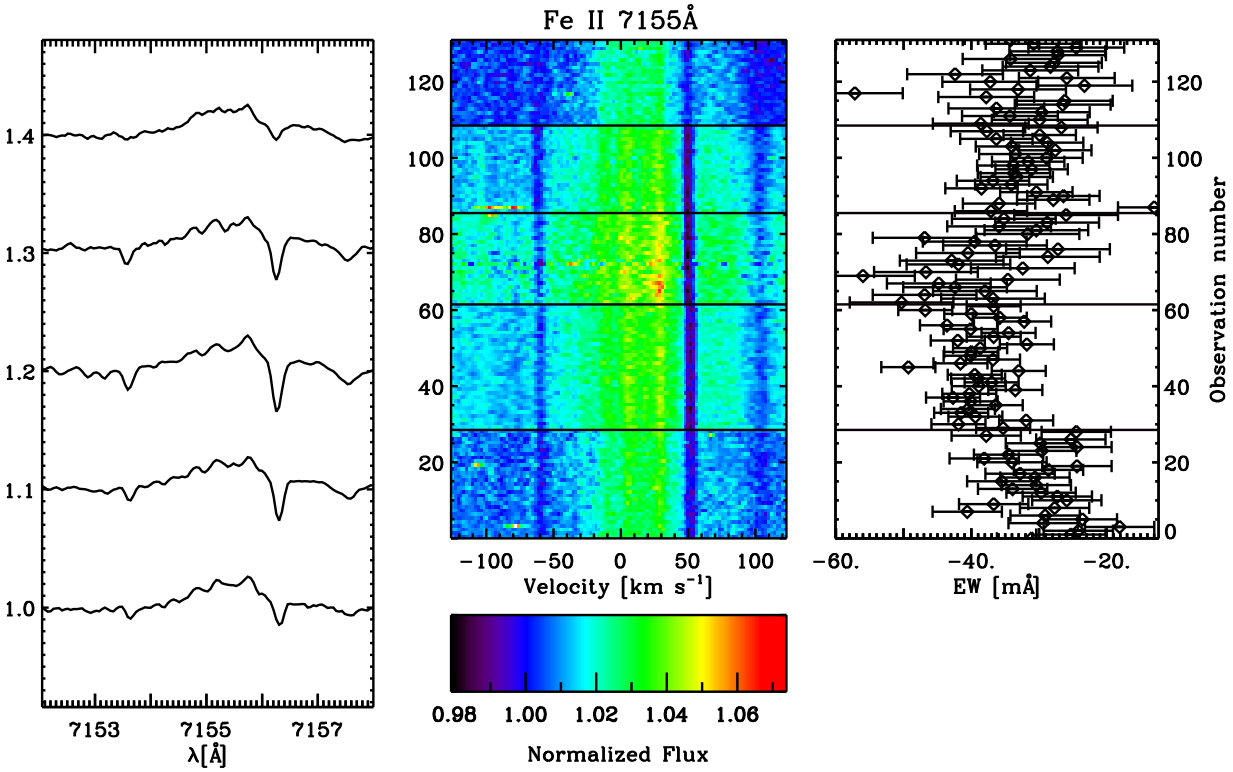

FIG. 31.— HD 98922 Fe II 7155Å. As in Fig. 27. There is a telluric absorption line at 7156.27Å (Catanzaro 1997). Here we show only the emission component EW.

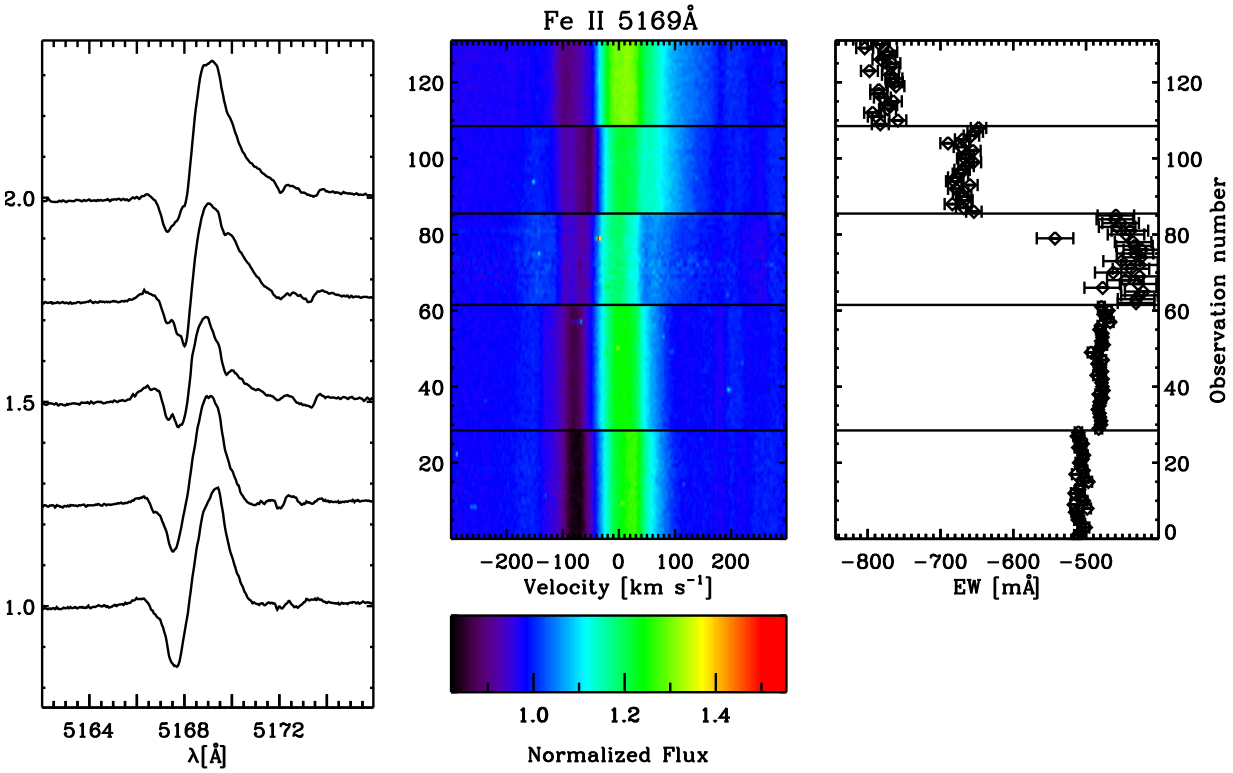

FIG. 32.— HD 98922 Fe II 5169Å. As in Fig. 27.

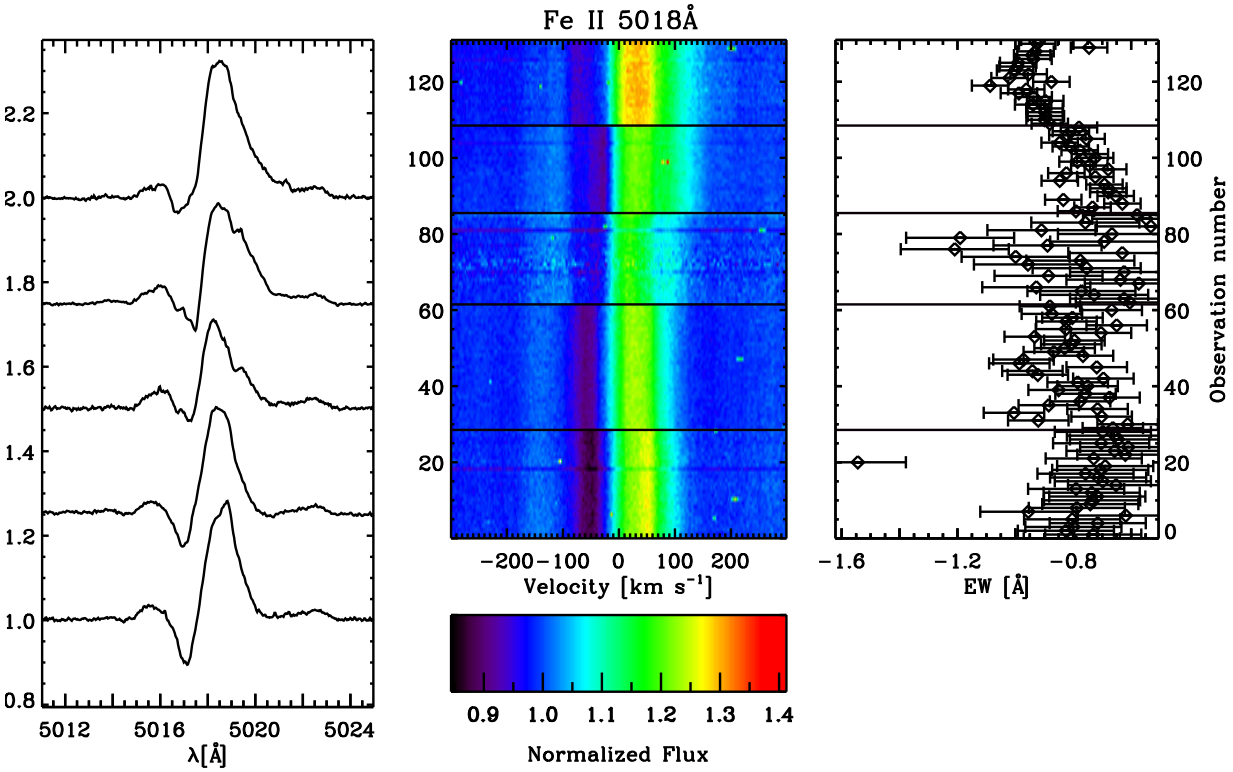

FIG. 33.— HD 98922 Fe II 5018Å. As in Fig. 27.

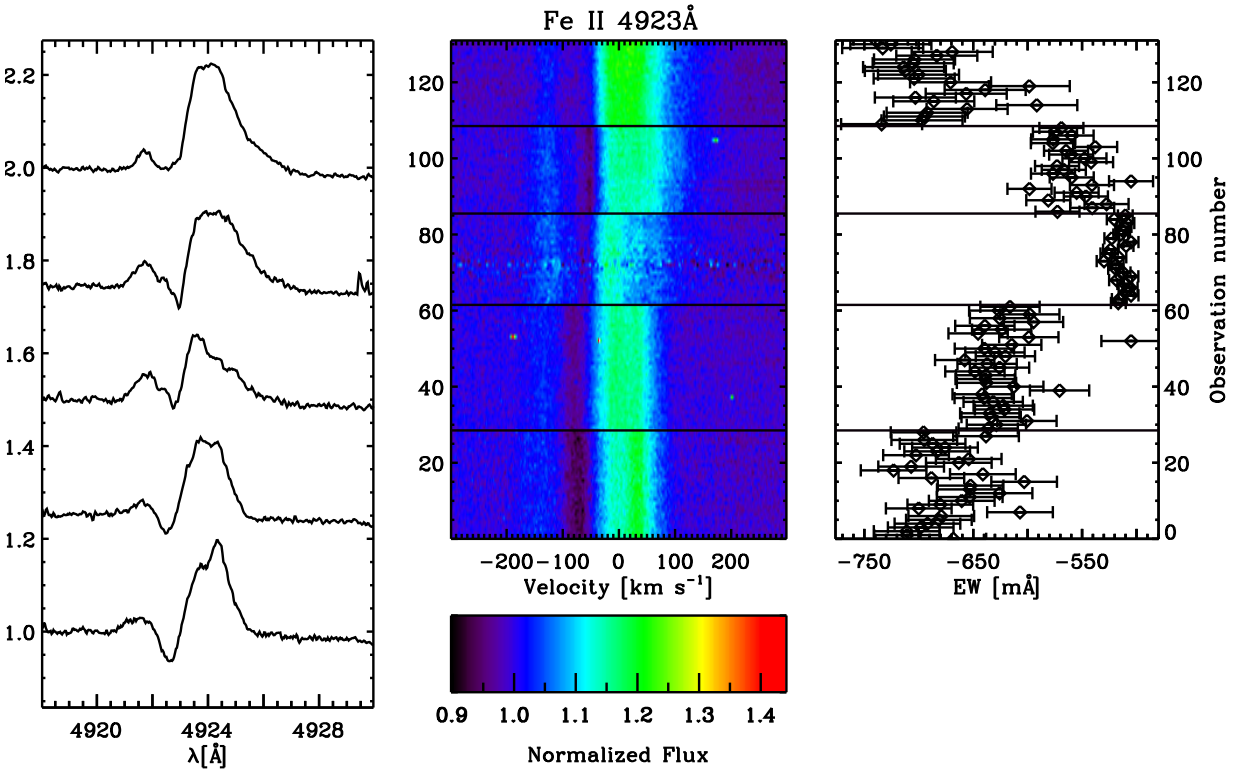

FIG. 34.— HD 98922 Fe II 4923Å. As in Fig. 27.

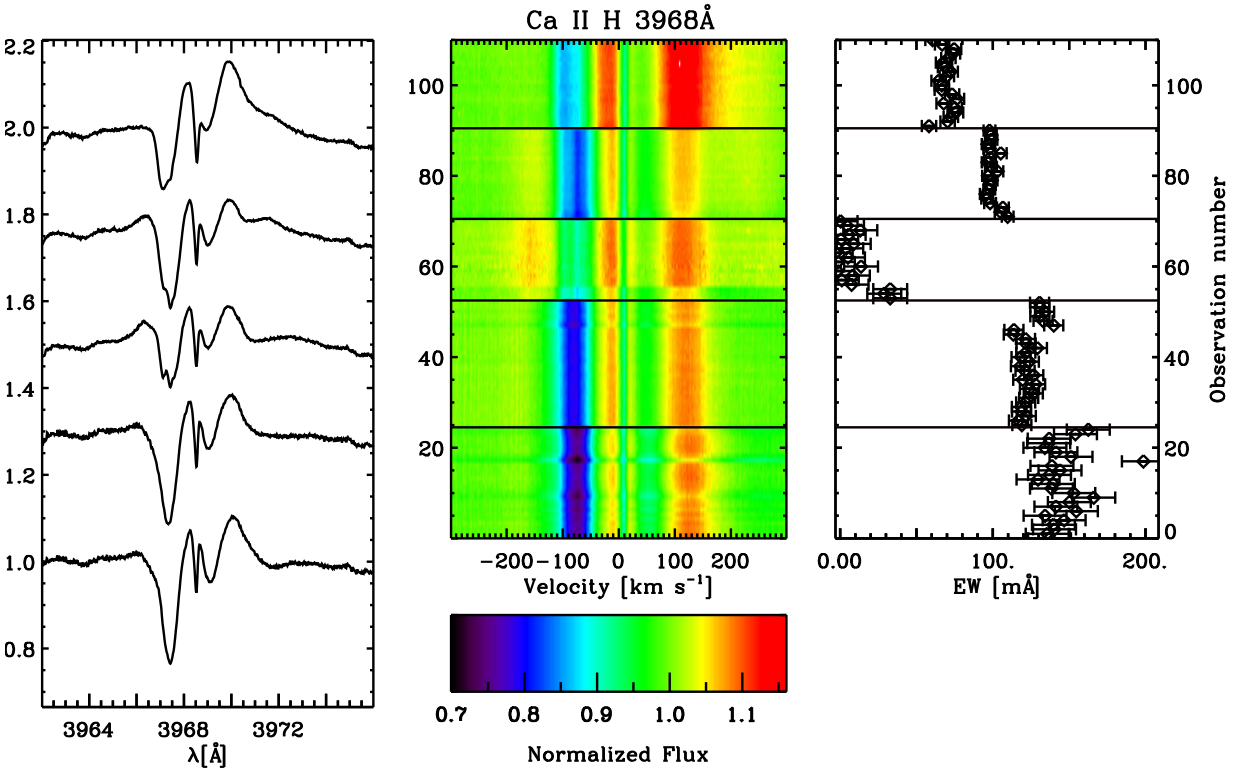

FIG. 35.— HD 98922 Ca II H 3968Å. As in Fig. 27.

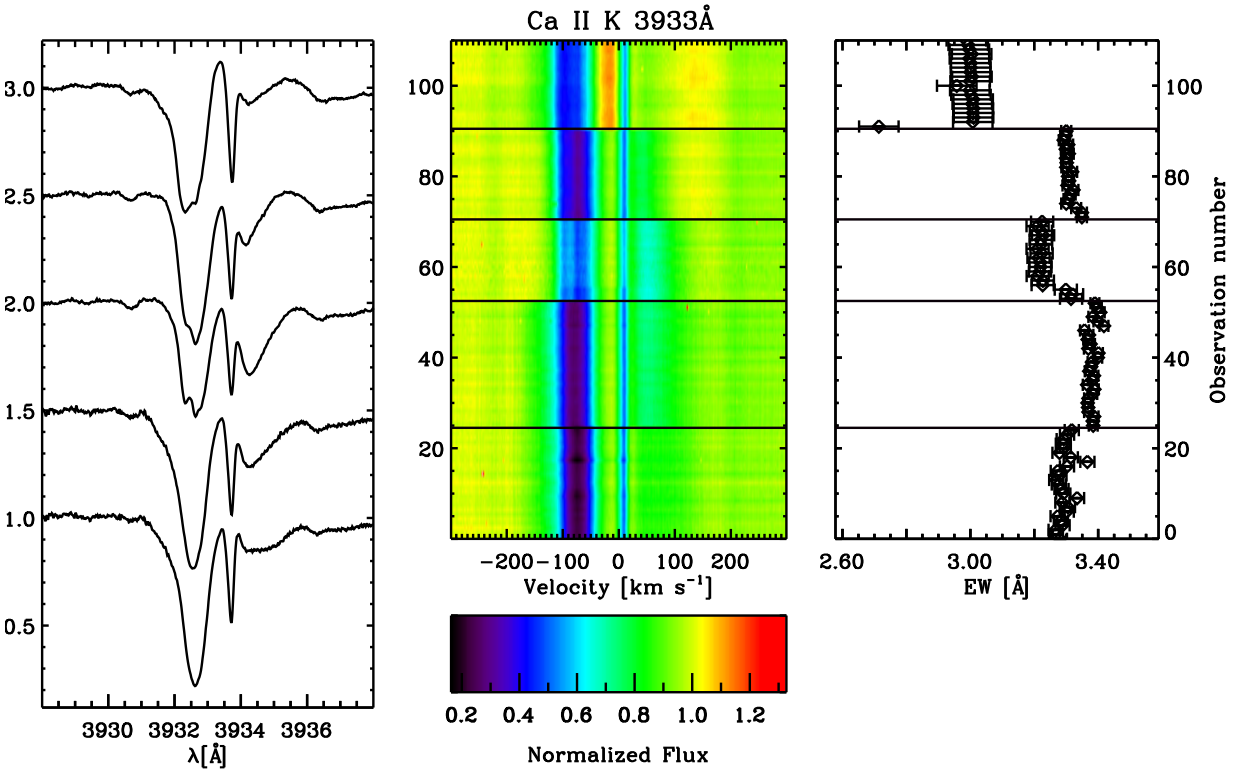

FIG. 36.— HD 98922 Ca II K 3933Å. As in Fig. 27.

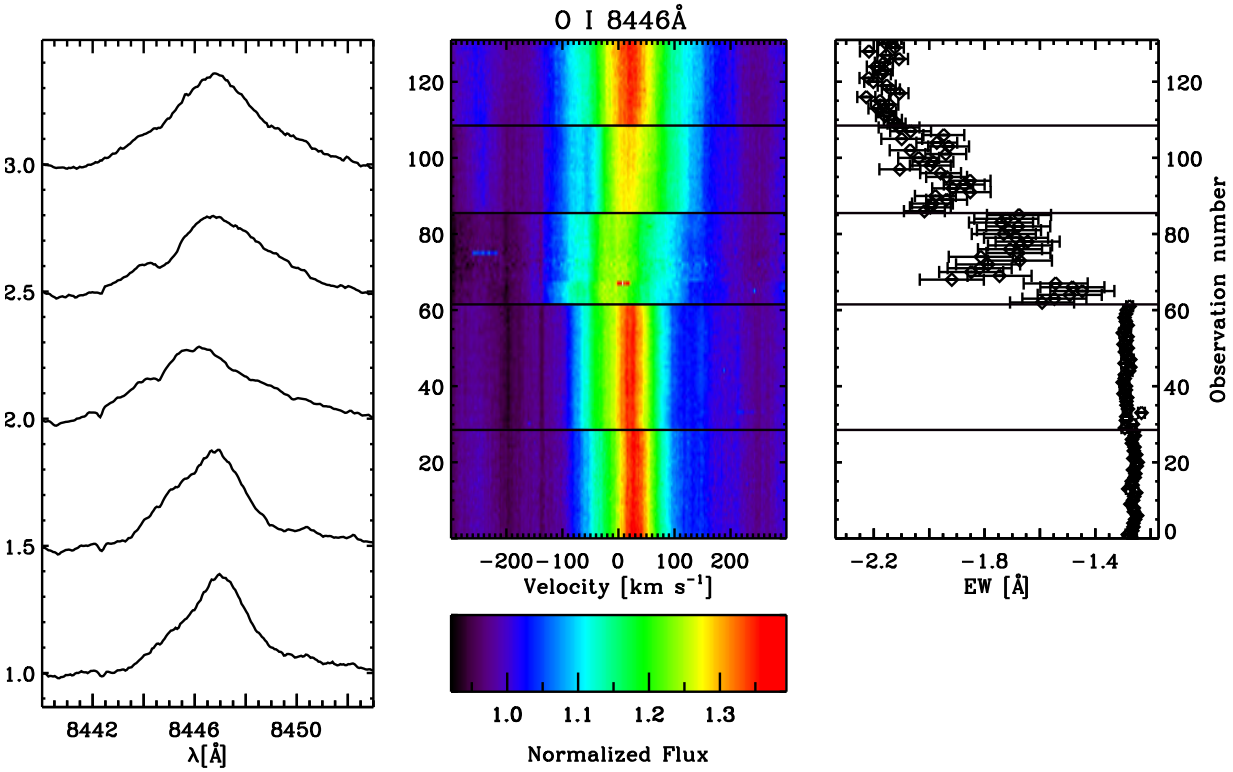

FIG. 37.— HD 98922 O I 8446Å. As in Fig. 27.

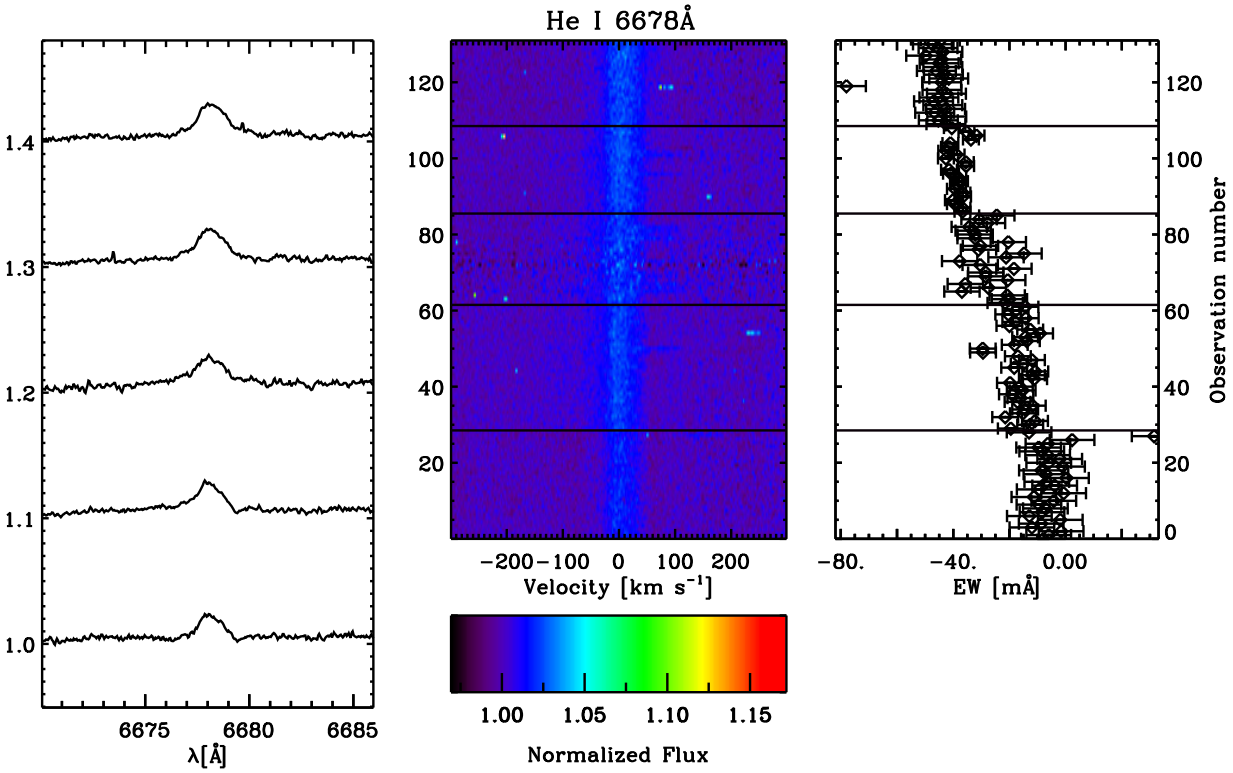

FIG. 38.— HD 98922 He I 6678Å. As in Fig. 27.

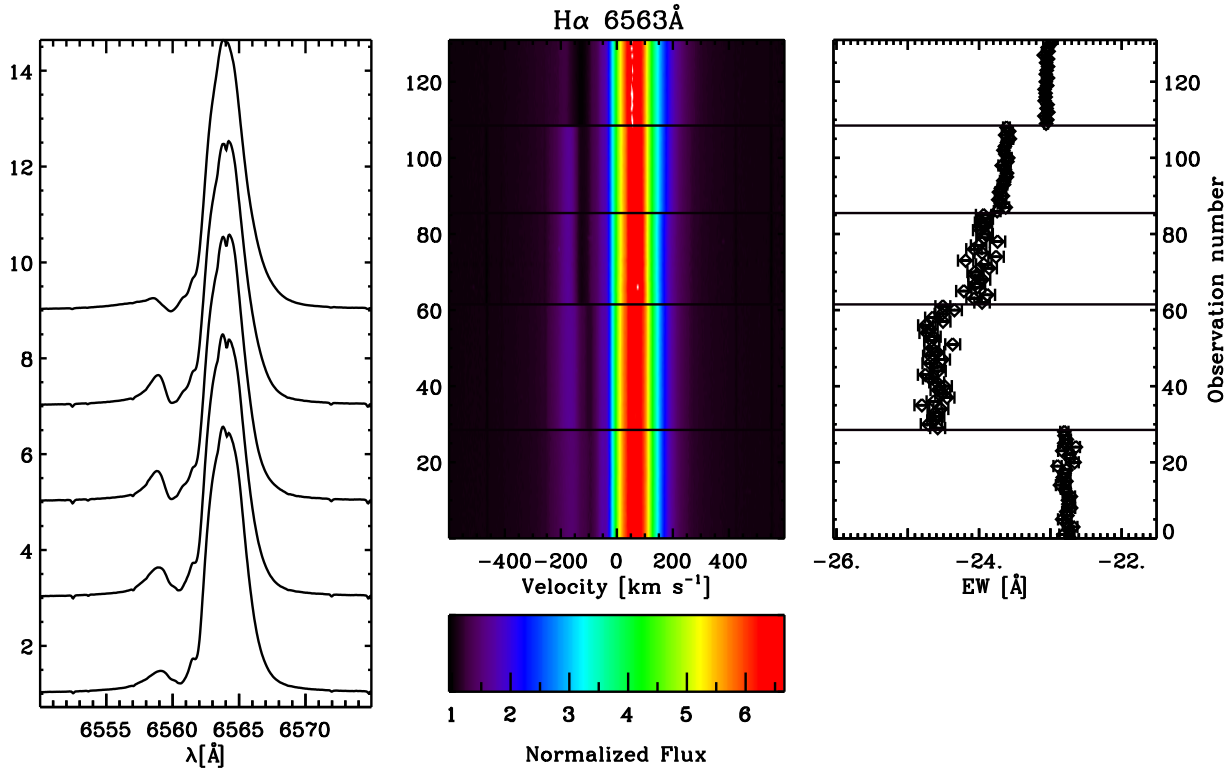

FIG. 39.— HD 98922 Hα. As in Fig. 27. Here, we show just the fit emission components' EW for plot scaling purposes.

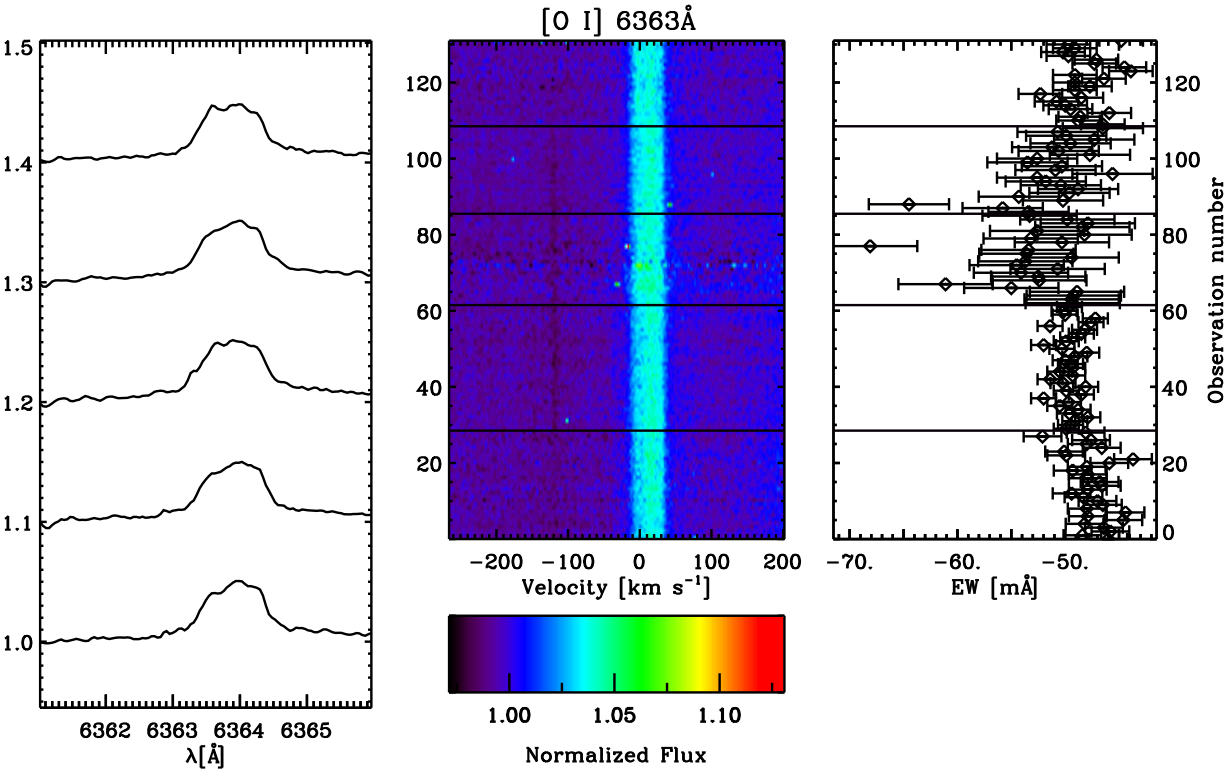

FIG. 40.— HD 98922 [O I] 6363Å. As in Fig. 27.

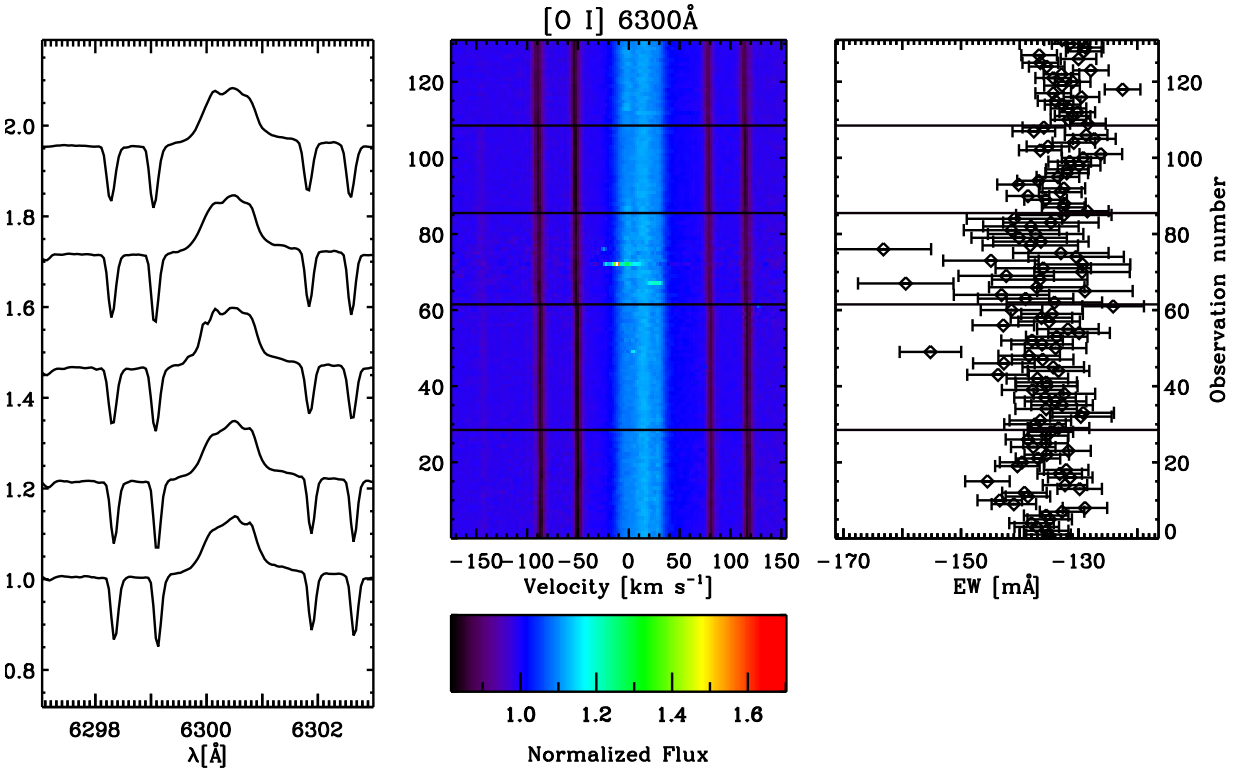

FIG. 41.— HD 98922 [O I] 6300Å. As in Fig. 27.

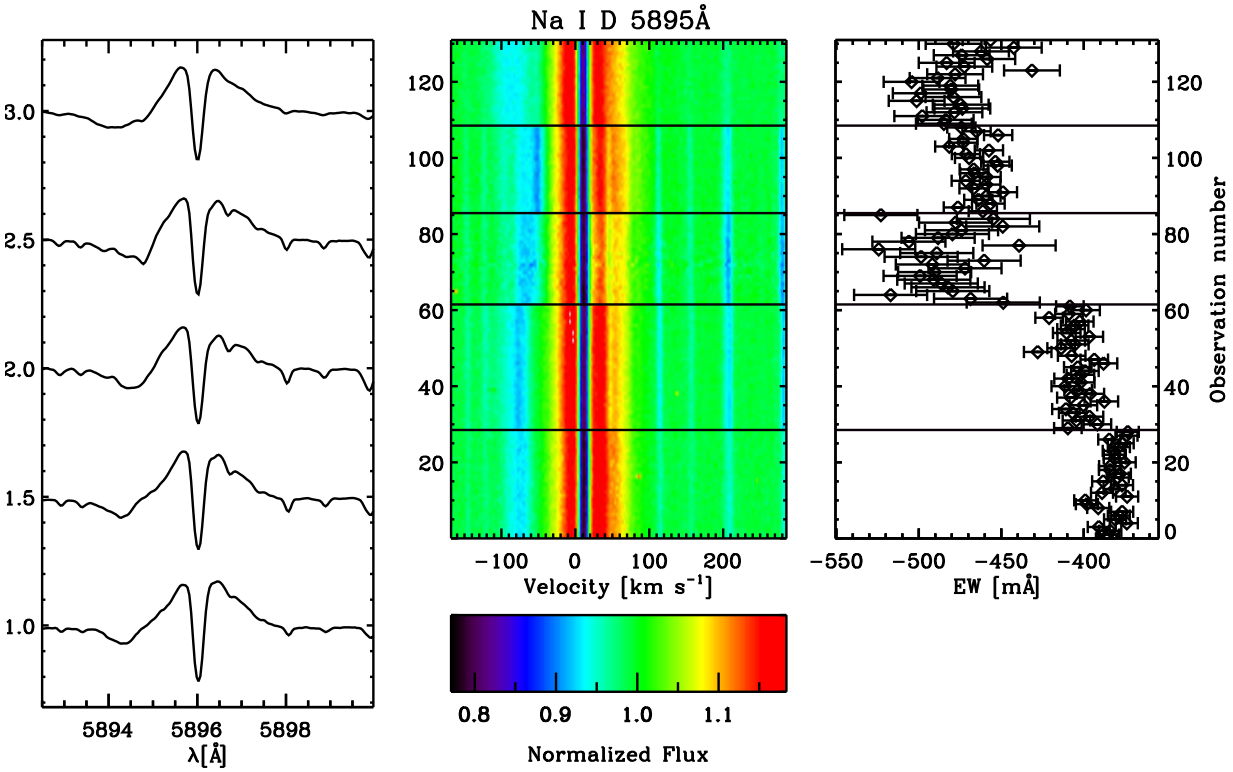

FIG. 42.— HD 98922 Na I 5895Å. As in Fig. 27.

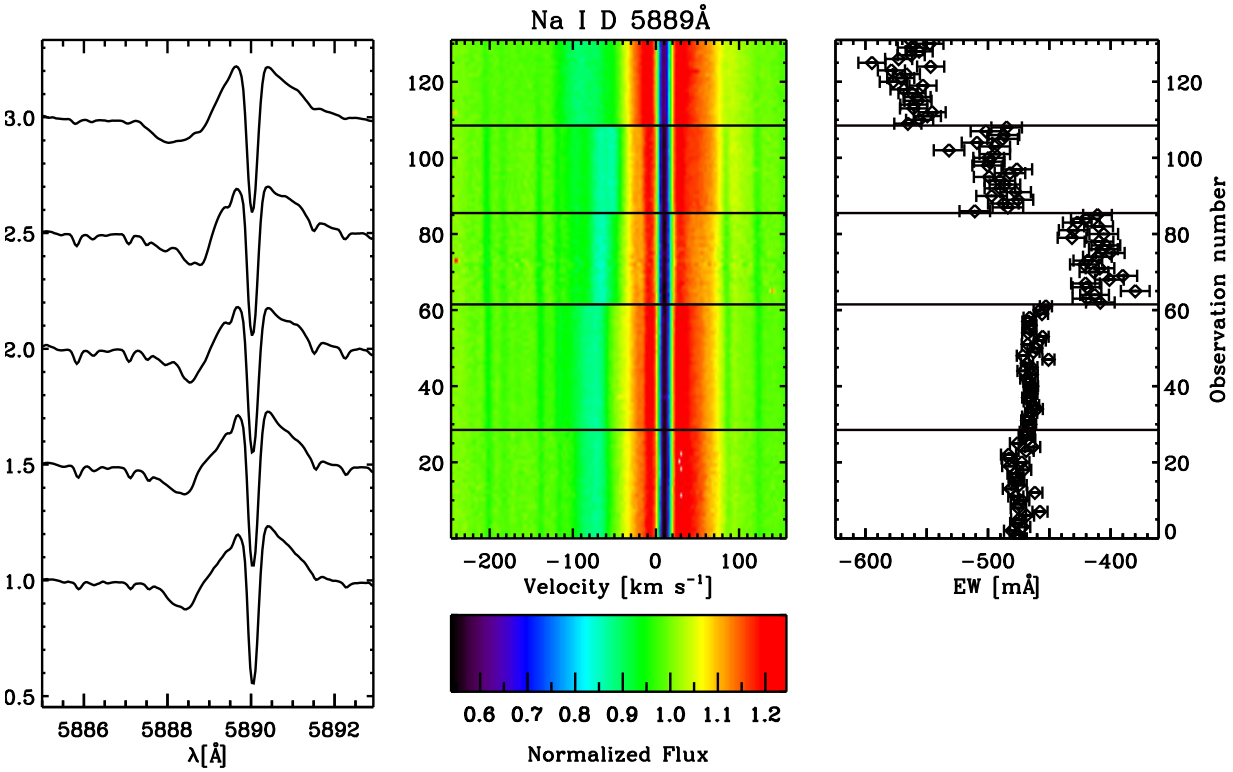

FIG. 43.— HD 98922 Na I 5889Å. As in Fig. 27.

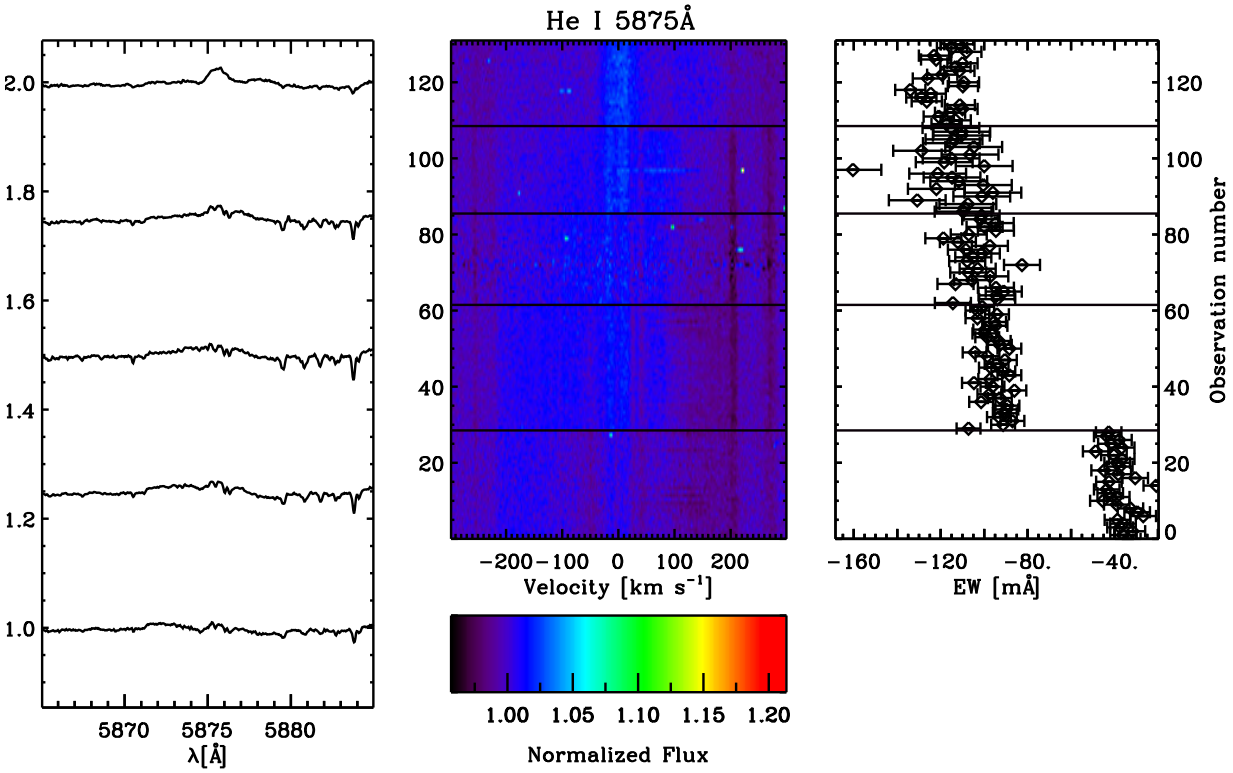

FIG. 44.— HD 98922 He I 5875Å. As in Fig. 27.

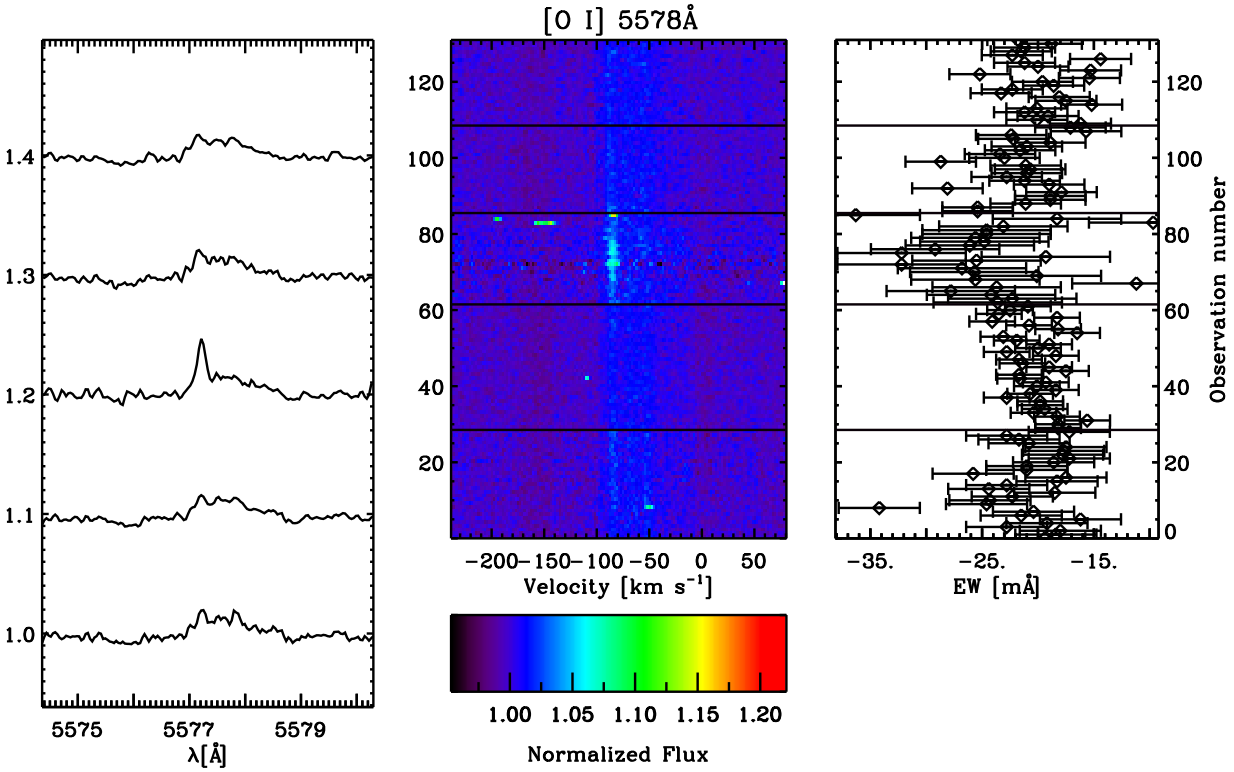

FIG. 45.— HD 98922 O I 5578Å. As in Fig. 27. Due to its persistence, we suggest the weak, broad emission line is stellar or circumstellar in origin. The narrow component that arises and fluctuates within the third night we believe to be airglow (Louistisserand et al. 1987).

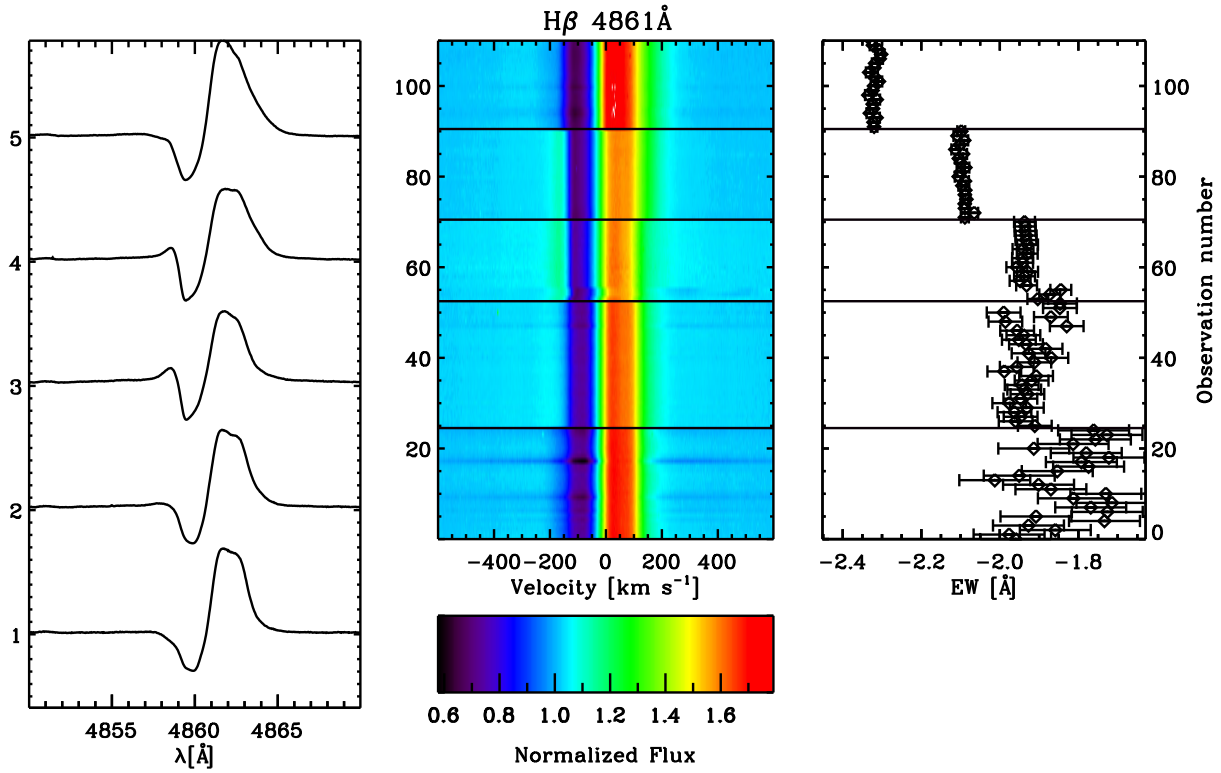

FIG. 46.— HD 98922 Hβ. As in Fig. 27. Here, we show just the fit emission components' EW for plot scaling purposes.

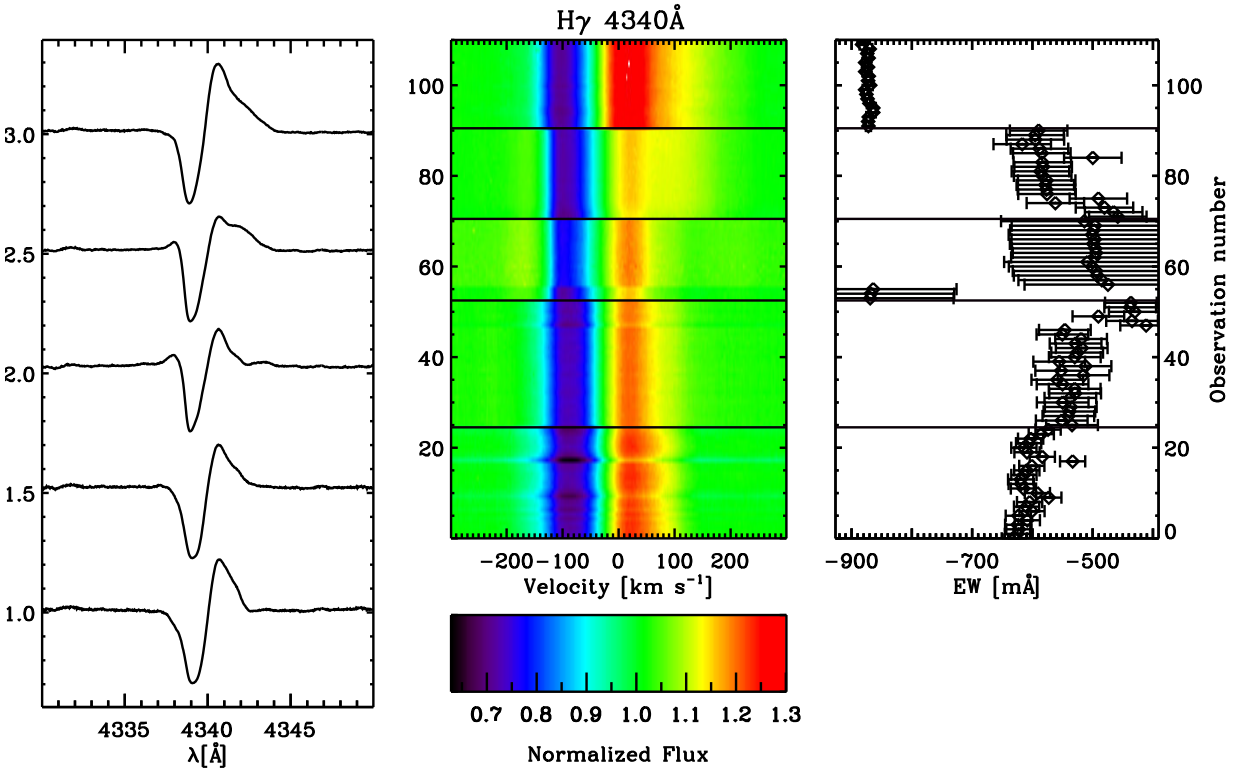

FIG. 47.— HD 98922 Hγ. As in Fig. 27. Here, we show just the fit emission components' EW for plot scaling purposes.

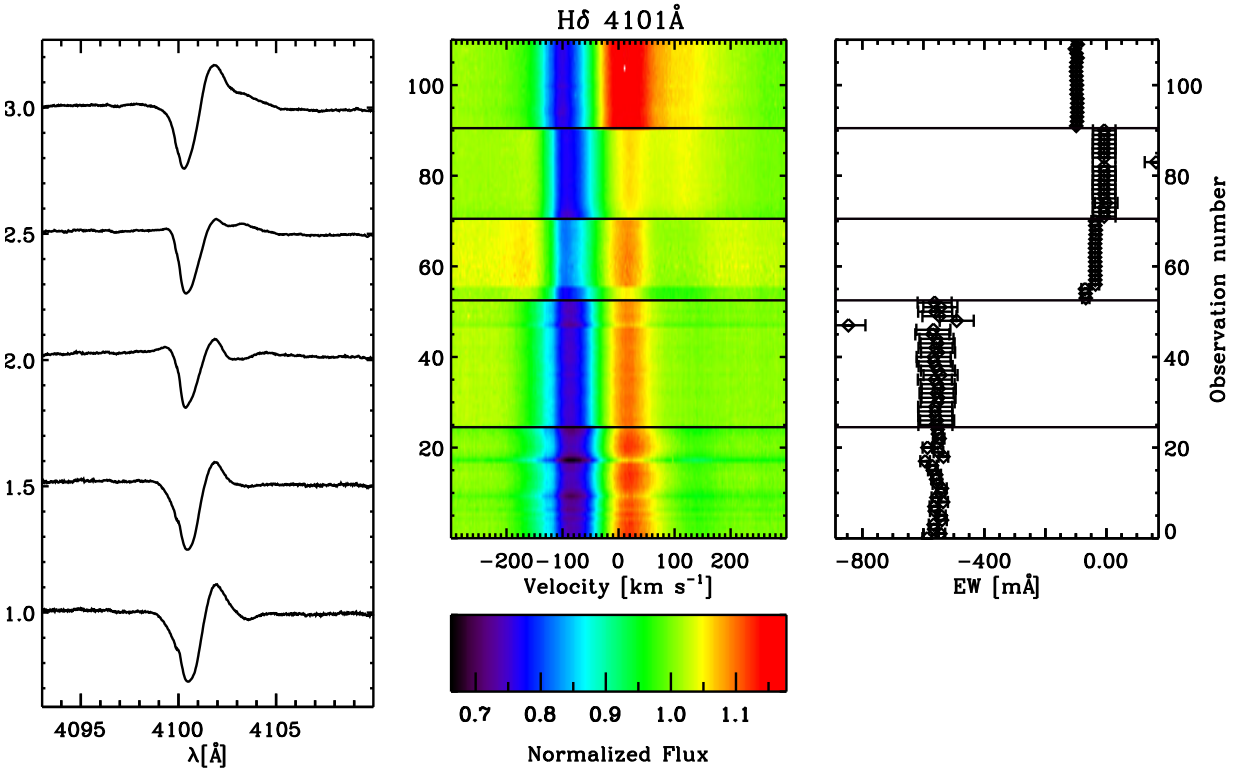

FIG. 48.— HD 98922 Hδ. As in Fig. 27. Here, we show just the fit emission components' EW for plot scaling purposes.

TABLE 3
Adopted TORUS model parameters

	V1295 Aql		HD 98922	
System inclination [°]	10, 34		45	
	Herbig-like	T Tauri-like	Herbig-like	T Tauri-like
Magnetosphere parameters				
R_{inner} [R_*]	1.0	3.0	···	3.0
R_{outer} [R_*]	1.3	4.4	···	4.1
T_{max} [K]	8000	8000	···	8000
$\dot{M}_{acc}$ [$M_\odot$ yr^{-1}]	10^{-5}	10^{-7}, 10^{-8}	···	10^{-6}
Disk wind parameters				
$\dot{M}_{wind}$ [$M_\odot$ yr^{-1}]	10^{-8}		10^{-7}	
T_{wind} [K]	8000		8000	
R_{inner} [R_*]	4.4		4.1	
R_{outer} [R_*]	10		10, 20	
θ [°]	30		30	

Note. — Key parameters of the magnetosphere and disk wind for our models of V1295 Aql and HD 98922. Adopted stellar parameters appear in Table 2. We have assumed a magnetospheric temperature structure as described in Hartmann et al. (1994), defining T_{max} for both stars as 8000 K. We assume an isothermal disk wind, and θ is the wind half-opening angle with respect to the stellar rotation axis. For all wind models, we set wind acceleration parameter β to 0.2 and the acceleration length scale to 10 times the inner wind launching radius (cf. Kurosawa et al. 2006, and references therein). References and derivation of these values discussed in sections devoted to each star.

B. TORUS MODELS OF V1295 AQUILA AND HD 98922

Model setup

As a means for exploring mechanisms for line formation in the systems we observed, we have calculated line transfer with TORUS for systems comprised of a star, magnetosphere, disk, and disk wind. The modular framework of TORUS as applied to star+disk systems is described in more detail in Kurosawa et al. (2006); we highlight salient details for our Herbig AeBe-specific application below. Our TORUS models calculate level populations by solving the rate equations for Hydrogen assuming non-LTE conditions. Doppler broadening is applied to the line profiles assuming turbulent velocity in the flow of 20 km s^{-1}; pressure broadening as formulated in Muzerolle et al. (2001) is also applied and is the dominant broadening mechanism for the lines we study here.

The radial extent at which a dipolar field of a given strength can hold off infall (Koenigl 1991), r_T, is expressed (using the formulation of Hartmann 1998) as:

$$\frac{r_T}{R_*} = 3.7 B_3^{4/7} \dot{M}_{-7}^{-2/7} M_{1/2}^{-1/7} R_2^{5/7}; \tag{B1}$$

where B_3 is the magnetic field strength in units of kG, $\dot{M}_{-7}$ is the mass accretion rate in units of 10^{-7} $M_\odot$ yr^{-1}, $M_{1/2}$ is the stellar mass in units of 0.5 $M_\odot$, and R_2 is the stellar radius in units of 2 $R_\odot$.

For a fiducial case, we use parameters for the one object we study here with a detected magnetic field, V1295 Aql. For its measured ∼100 G field, stellar parameters as reported in Table 2 and an observationally determined accretion rate of $\sim 10^{-5}$ $M_\odot$ yr^{-1} (Mendigutía et al. 2011b) this magnetospheric radius is 0.32 R_*. To compare this to a T Tauri-like case, we also compute models with magnetospheres truncated where a 1kG field would imply. For HD 98922 it is 4.1 R_*, and for V1295 Aql, we have tested various accretion rates and their corresponding magnetospheric truncation radii; we discuss our preferred lower accretion rate (10^{-7} and 10^{-8} $M_\odot$ yr^{-1}) models with magnetospheres truncated at 4.4 R_* below. For both stars, we set the inner edge of the dust disk to their respective sublimation radii and the disk wind half-opening angle to 30° with respect to the stellar rotation axis; interior to this is an optically thick gaseous disk component that extends to the magnetosphere edge where the disk wind launches.

In Table 3, we summarize key parameters adopted in our models and discuss for each star below how they were chosen and the impact on the line profiles of their adjustment. In Fig. 49, we show calculated Hα and Hβ line profiles for cases we refer to as "Herbig-like" (with small/no magnetospheres) and "T Tauri-like" (with magnetospheres derived assuming 1kG fields). Overall, we found a magnetospheric component necessary to produce the observed emission lines but note other choices that could mimic this effect.

V1295 Aql

Very narrow photospheric lines and little modulation of photometric and spectropolarimetric signals indicate either low inclination or a very long rotation period for V1295 Aql (Eisner et al. 2004; Isella et al. 2006; Catala et al. 2007). Interferometric values reported in the literature poorly constrain system inclination: 12-65° values are gotten (though the sparse $u-v$ coverage of both Eisner et al. 2004 and Isella et al. 2006 does not permit ruling out a pole-on view or binarity) while Ragland et al. (2012) derive a highly inclined 72°. For our TORUS models, we adopt 34° from analysis of new PIONIER data Lazareff et al. (2017) and assess the line profile structure's dependence on inclination.

Assuming an accretion rate of 10^{-5} $M_\odot$ yr^{-1} and magnetic field strength of 100 G, we derive a magnetospheric extent of 0.32 R_*. In this "Herbig-like" model, we find weak contribution to the line profile (Figure 49, upper left panel); emission and absorption components at ∼10% of the continuum level are much weaker than observed in our spectra. At 10° inclination, higher velocity blueshifted material is all that is observed of the magnetospheric emission, its peak overlapping with the broad, faster, wind emission in Hα but readily visible at ~ -70 km s^{-1} in Hβ. At an inclination of 34°, more of the accretion stream is visible–notably, the low-velocity material–and a distinct emission peak is seen near 0 km s^{-1}. In Figure 49 (upper left panel), we show a potentially unrealistically low disk wind mass loss rate given the high stellar accretion rate adopted; our purpose here is to visually isolate the profile of the same wind component used in the T Tauri-like case for demonstration. We note that at higher disk wind mass loss rates, e.g. at 10% of the mass accretion rate, the disk wind itself is redshifted from line center and dominates the overall emission profile, its peak stronger than is observed in our data.

To model a T Tauri-like case, we tested an extended dipolar magnetosphere reaching from 3-4.4 R_*. We performed tests for various inner magnetospheric radii and accretion rates to then reproduce the overall emission strength and velocity width observed in our spectra and assessed line profiles at various potential system inclination angles. We found a more modest mass accretion rate of 10^{-7} $M_\odot$ yr^{-1}, a couple orders of magnitude lower than that reported in the literature, and an outer magnetospheric radius of 4.4 R_* (calculated assuming 1kG field) was able to reproduce comparable emission in the modeled lines to our observations (Figure 49, top right panel; black solid/dashed line profiles). A higher mass accretion rate as reported in the literature from a study not done in the same epoch as our observations combined with a more extended magnetosphere as is modeled here produced stronger emission than we observed; interestingly, for the parameter spaces we explored, lower accretion rates of $\sim 10^{-7}-10^{-8} M_\odot$ yr^{-1} and smaller magnetospheric sizes produce strikingly similar profiles to our observations.

In Figure 49, upper right panel, red solid and dashed lines, we show the exact same model with an accretion rate one order of magnitude lower (10^{-8} $M_\odot$ yr^{-1}) and note the line profile peak asymmetry shift from higher on the blue side of the line to higher on the red side of the line and an overall decrease in line strength more consistent with our observations. Generally, we find in our models that higher accretion rates and more extended magnetospheres (i.e., with inner radii set closer to the star) produce more symmetric profiles about the line's peak flux while more compact magnetospheres generate asymmetric peaks. These asymmetries manifest at low accretion rates as the distinctive, narrow, enhanced redward emission peak shape like observed in V1295 Aql. Uncertainty in the Balmer excess measurement (the difference in flux in the U and B bands) of 0.1-0.2 dex can lead to one to two orders of magnitude uncertainty in the accretion rate, making our models' low accretion rates consistent with the measurements. The line profiles observed by us during this epoch indicate it is highly unlikely either object observed is in a high mass accretion rate regime, as the line wings are relatively narrow (±200 km s−1) and the continuum opacity is not high enough to have driven the lines into absorption (e.g., the high temperature, high $\dot{M}$ models in Muzerolle et al. 2001). Finally, we also note the stellar mass cited by Mendigutía et al. (2011b) is a factor of 2 higher than our adopted value; a revised stellar mass would likely lead to a lower mass accretion rate derived via the accretion shock models.

While the structure in the Hα emission profile is highly suggestive, we are only able to produce the line profile at relatively low system inclinations ranging from 10°-34°. Even so, the models' redshifted absorption is not present in the observed spectra and we are unable to reproduce the blueshifted absorption observed. Since we have used an unrealistically large magnetosphere as a fiducial model (when the 100 G field strength and high measured mass accretion rate implies a <1 R_* extent), a substantial fraction of the emission could be originating from a hot, inner gaseous disk or a spherically symmetric wind launched from within a few stellar radii of the star. Indeed, Catala et al. (2007) were able to model the Hα line using a stellar wind and note the similarity between the observed profile and a familiar P Cygni profile. This is to say there is a substantial degeneracy in modeling these line profiles: a stellar wind with a compact launch/emission region can mimic the appearance of a magnetosphere. Modeling of these systems requires information about the stellar magnetic field to break these degeneracies. Finally, at the low system inclination at which a magnetosphere closest matches the emission line profile, in order to produce the observed blueshifted absorption, a disk wind launching angle steeper than the critical angle beyond which a flow cannot be initiated (e.g., 30° from the disk normal vector Blandford & Payne 1982) would need be invoked. We tested various disk wind geometries, varying the half-opening angle from 30°-45° and the width of the wind launching region (which then changes the density along the line of sight) and even for the most shallow half-opening angle and narrowest case tested (shown in Figure 49), no blueshifted absorption was produced. Thus, we conclude a stellar wind scenario is more consistent with all of the data available to us.

HD 98922

In Figure 49 we present "Herbig-like" and "T Tauri-like" models of HD 98922 in the left and right bottom panels respectively; the left panel is simply the same model as in the right, but with the magnetosphere component turned off.

For HD 98922, we performed a similar calculation of the magnetospheric truncation radius assuming a TTS-like, 1kG field and adopting a mass accretion rate of rate of 10^{-6} $M_\odot$ yr^{-1} (Garcia Lopez et al. 2006); these parameters set the outer magnetospheric radius to 4.1 R_*. We initially adopted parameters from the literature for the disk wind, including an isothermal temperature of 10,000 K (Caratti o Garatti et al. 2015) and a disk wind mass loss rate of 10^{-7} $M_\odot$ yr^{-1}, an order of magnitude lower than the accretion rate (consistent with the model of Caratti o Garatti et al. 2015). In these models, we also initially chose a system inclination of 20° and disk wind half opening angle (with respect to

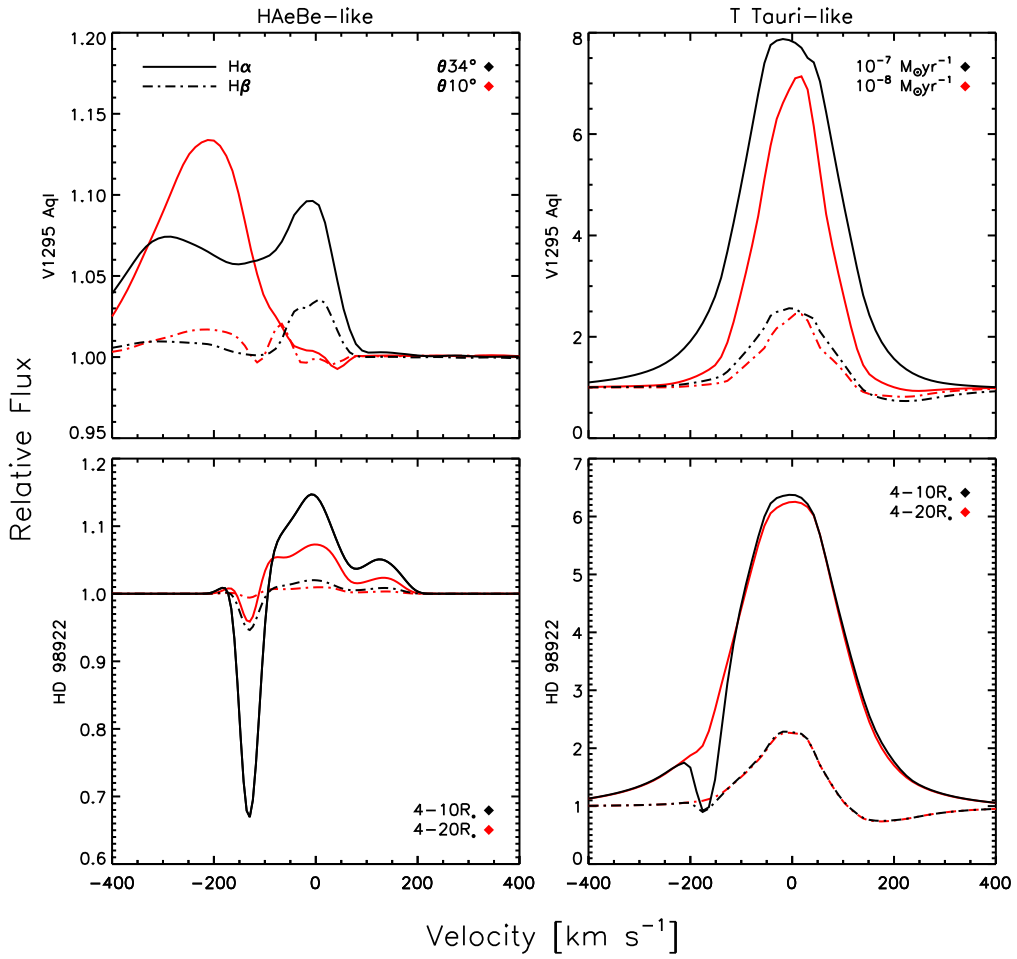

FIG. 49.— Our TORUS model spectra comparing small/no magnetosphere models ("HAeBe-like," left column) and extended magnetospheres assuming 1kG fields ("T Tauri-like," right column) for V1295 Aql (top row) and HD 98922 (bottom row). We present Hα (solid) and Hβ (dot-dashed) profiles; for V1295 Aql, we show the effect of system inclination and mass accretion rate choice on the line profiles, and for HD 98922 we demonstrate how the size of the wind launching region effects absorption depth. For the T Tauri-like cases, an inverse P Cygni profile is present in Hα and becomes readily apparent in the Hβ profiles, in disagreement with the observed spectra at all epochs. Model parameters are summarized in Table 3.

the stellar rotation axis, assumed to be perpendicular to the disk) of 30° as done by Caratti o Garatti et al. (2015), but find the disk wind does not provide enough opacity along the line of sight and thus doesn't produce blueshifted absorption observed in our spectra. In the models shown here, therefore, we adopt the 45° system inclination reported by Blondel & Djie (2006). We found at this steeper inclination a 10,000 K disk wind still did not absorb; we adjusted the wind temperature until it did begin to absorb at 8000 K and have set the temperature to that value in all models shown here. We note an even cooler still 7000 K disk wind produces very deep absorption, to ∼0.01% of the continuum level, which we do not observe an any epoch of our spectra.

At its slightly higher system inclination, we are easily able to produce blueshifted absorption in the HD 98922 models with a disk wind. In Figure 49 (bottom two panels), we show the effect of changing the disk wind launching region width on the depth of the absorption profile. A narrower launch region increases density along the line of sight and produces deeper absorption. This effect can be mimicked by altering the system inclination or the mass loss rate. We have calculated observationally and physically motivated models without a magnetosphere, as would be suggested by the non-detection of this object in spectropolarimetric surveys, but found no combination of disk wind or hot inner disk components able to produce substantial emission above the continuum level; indeed, the disk wind itself produces a multiply-peaked profile not observed in any line in our spectra (Figure 49, lower left panel).

Our T Tauri-like line profile models for HD 98922 (Fig. 49) are better able to reproduce observations than in the case of V1295 Aql, though we find the depth of the disk wind absorption highly dependent on the disk wind launching region extent. Additionally, with a symmetric disk wind, we are unable to reproduce the multiple absorption components and substructure observed in our spectra. This model, while it coarsely resembles our data, includes a magnetosphere and its attendant inverse P Cygni absorption which is not physically realistic given the magnetic field non-detection status of HD 98922. It is unclear what could be producing the observed emission, though a source spatially compact and

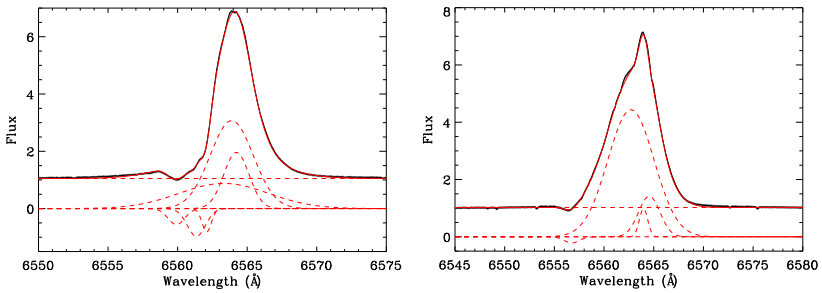

FIG. 50.— Gaussian profile fits to observed Hα lines of HD 98922 (left) and V1295 Aql (right) using Peak ANalysis (PAN). Individual fit components (red, dashed lines) and total fit (red, solid line) are shown along with a single observed line profile (black, solid line).

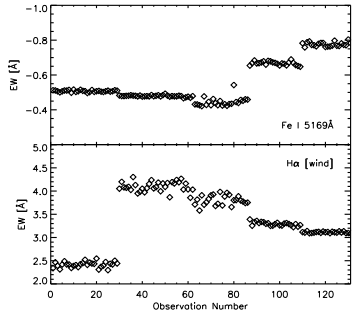

FIG. 51.— Comparison of the time evolution of the Fe II (42) 5169Å emission line compared to the wind absorption component of Hα in HD 98922. As the Fe II emission strengthens (increasingly negative equivalent width, per convention), the Hα wind absorption is growing weaker. Here (and in Figures 3 and 4), we have accounted for sign convention and see this represented as anticorrelation with a coefficient of -0.53.

close to the star that is unlikely to be a magnetosphere could be invoked. A more complex disk wind, incorporating asymmetric regions and temperature stratification, could be imagined.

A combination of factors suggest a disk wind is producing the observed features in HD 98922: the interferometrically determined system inclination provides a more favorable geometry for a disk wind to cross our line of sight, and the escape velocity in the blueward absorption component of the spectral lines is lower than the stellar escape velocity ($v_{esc}\sin i \sim$295 km s^{-1}) and thus more consistent with a radius farther from the star.

C. TIME EVOLUTION OF LINE COMPONENT EQUIVALENT WIDTHS AND ABSORPTION FEATURE SUBSTRUCTURE

As described in Section 3, we performed line profile analysis by fitting Gaussian and background functions to our spectral line profiles in order to determine the overall line equivalent width and to assess potential substructures contributing to the line profile. In Figure 50 we show an example of this technique for Hα line profiles of HD 98922 and V1295 Aql.

Here, in Figure 51, we supply an example demonstrating the time-evolving equivalent width correlation calculations as seen in Figs. 3 and 4. The Hα data are non-monotonic between the first two nights, but our test statistic detects and returns that the bulk of the EW evolution is monotonic and anticorrelated with Fe II (42) 5018Å.

Both static and evolving features are observed within the absorption components of Hα in V1295 Aql and HD 98922 (Fig. 52). These features, seen both in emission and absorption, are not telluric in origin. We have employed a local minimum and maximum finding algorithm in order to quantify the velocity evolution of these features. Potentially, static components could be associated with slower-evolving disk wind structure, while the higher velocity accelerating and decelerating features could be structures in faster-moving flow like a stellar wind.

REFERENCES

Acke, B., van den Ancker, M. E., & Dullemond, C. P. 2005, A&A, 436, 209
Acke, B., & Waelkens, C. 2004, A&A, 427, 1009
Alecian, E., Neiner, C., Mathis, S., Catala, C., Kochukhov, O., & Landstreet, J. 2013a, A&A, 549, L8
Alecian, E., Wade, G. A., Catala, C., Grunhut, J. H., Landstreet, J. D., Böhm, T., Folsom, C. P., & Marsden, S. 2013b, MNRAS, 429, 1027
Alecian, E., et al. 2013c, MNRAS, 429, 1001
Bai, X.-N., & Stone, J. M. 2013, ApJ, 769, 76
Bernstein, R., Shectman, S. A., Gunnels, S. M., Mochnacki, S., & Athey, A. E. 2003, in Society of Photo-Optical Instrumentation Engineers (SPIE) Conference Series, Vol. 4841, Instrument Design and Performance for Optical/Infrared Ground-based Telescopes, ed. M. Iye & A. F. M. Moorwood, 1694–1704
Bernstein, R. M., Burles, S. M., & Prochaska, J. X. 2015, PASP, 127, 911
Blandford, R. D., & Payne, D. G. 1982, MNRAS, 199, 883
Blondel, P. F. C., & Djie, H. R. E. T. A. 2006, A&A, 456, 1045
Caratti o Garatti, A., et al. 2015, A&A, 582, A44
Catala, C., et al. 2007, A&A, 462, 293
Catanzaro, G. 1997, Ap&SS, 257, 161
Cauley, P. W., & Johns-Krull, C. M. 2014, ApJ, 797, 112

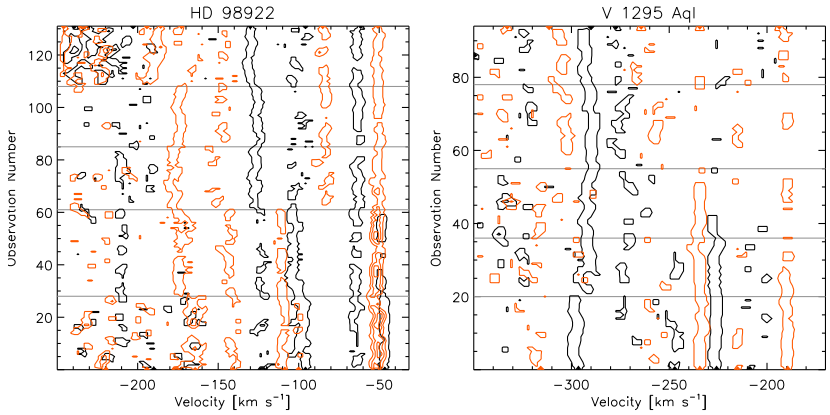

FIG. 52.— Tracing weak absorption (black contours) and emission components (orange contours) within the blueshifted absorption of HD 98922 (left) and V1295 Aql (right). While noise does interfere with the tracing of these weak features, several distinct velocity components persist over multiple nights of observation (demarcated by horizontal lines), either remaining static at one velocity or evolving over the course of our observations.

Corcoran, M., & Ray, T. P. 1998, A&A, 331, 147
Costigan, G., Vink, J. S., Scholz, A., Ray, T., & Testi, L. 2014, MNRAS, 440, 3444
Eisner, J. A., Lane, B. F., Hillenbrand, L. A., Akeson, R. L., & Sargent, A. I. 2004, ApJ, 613, 1049
Ellerbroek, L. E., et al. 2015, A&A, 573, A77
Ferreira, J. 2013, in EAS Publications Series, Vol. 62, EAS Publications Series, 169–225
Ferreira, J., Dougados, C., & Cabrit, S. 2006, A&A, 453, 785
Garcia Lopez, R., Natta, A., Testi, L., & Habart, E. 2006, A&A, 459, 837
Gregory, S. G., Donati, J.-F., Morin, J., Hussain, G. A. J., Mayne, N. J., Hillenbrand, L. A., & Jardine, M. 2012, ApJ, 755, 97
Hales, A. S., et al. 2014, AJ, 148, 47
Harries, T. J. 2000, MNRAS, 315, 722
Hartigan, P., Edwards, S., & Ghandour, L. 1995, ApJ, 452, 736
Hartmann, L. 1998, Cambridge Astrophysics Series, 32
Hartmann, L., Hewett, R., & Calvet, N. 1994, ApJ, 426, 669
Herbig, G. H. 1960, ApJS, 4, 337
Hubrig, S., Yudin, R. V., Schöller, M., & Pogodin, M. A. 2006, A&A, 446, 1089
Hubrig, S., et al. 2009, A&A, 502, 283
Isella, A., Testi, L., & Natta, A. 2006, A&A, 451, 951
Johns, C. M., & Basri, G. 1995, AJ, 109, 2800
Knigge, C., Woods, J. A., & Drew, J. E. 1995, MNRAS, 273, 225
Koenigl, A. 1991, ApJ, 370, L39
Kraus, S., Preibisch, T., & Ohnaka, K. 2008a, ApJ, 676, 490
Kraus, S., et al. 2008b, A&A, 489, 1157
Kurosawa, R., Harries, T. J., & Symington, N. H. 2006, MNRAS, 370, 580
Kurosawa, R., et al. 2016, MNRAS, 457, 2236
Kurucz, R. L. 2005, Memorie della Societa Astronomica Italiana Supplementi, 8, 189
Lazareff, B., et al. 2017, A&A, 599, A85
Long, K. S., & Knigge, C. 2002, ApJ, 579, 725
Louistisserand, S., Bucher, A., Koutchmy, S., & Lamy, P. 1987, A&AS, 68, 539
Mendigutía, I., Eiroa, C., Montesinos, B., Mora, A., Oudmaijer, R. D., Merín, B., & Meeus, G. 2011a, A&A, 529, A34
Mendigutía, I., Calvet, N., Montesinos, B., Mora, A., Muzerolle, J., Eiroa, C., Oudmaijer, R. D., & Merín, B. 2011b, A&A, 535, A99
Mora, A., et al. 2001, A&A, 378, 116
Munari, U., Sordo, R., Castelli, F., & Zwitter, T. 2005, A&A, 442, 1127
Muzerolle, J., Calvet, N., & Hartmann, L. 2001, ApJ, 550, 944
Muzerolle, J., D'Alessio, P., Calvet, N., & Hartmann, L. 2004, ApJ, 617, 406
Nguyen, D. C., Scholz, A., van Kerkwijk, M. H., Jayawardhana, R., & Brandeker, A. 2009, ApJ, 694, L153
Pogodin, M. A., Franco, G. A. P., & Lopes, D. F. 2005, A&A, 438, 239
Powell, S. L., Irwin, M., Bouvier, J., & Clarke, C. J. 2012, MNRAS, 426, 3315
Press, W. H., Teukolsky, S. A., Vetterling, W. T., & Flannery, B. P. 1992, Numerical recipes in FORTRAN. The art of scientific computing, 634
Ragland, S., et al. 2012, ApJ, 746, 126
Sousa, A. P., et al. 2016, A&A, 586, A47
Vink, J. S., Drew, J. E., Harries, T. J., & Oudmaijer, R. D. 2002, MNRAS, 337, 356
Wade, G. A., Bagnulo, S., Drouin, D., Landstreet, J. D., & Monin, D. 2007, MNRAS, 376, 1145
Weigelt, G., et al. 2011, A&A, 527, A103